

1 **Global three-dimensional simulation of Earth's dayside**
2 **reconnection using a two-way coupled magnetohydrodynamics**
3 **with embedded particle-in-cell model: initial results**

4 **Yuxi Chen¹, Gábor Tóth¹, Paul Cassak², Xianzhe Jia¹, Tamas I. Gombosi¹, James A.**
5 **Slavin¹, Stefano Markidis³, Ivy Bo Peng³, Vania K. Jordanova⁴, Michael G. Henderson⁴**

6 ¹Center for Space Environment Modeling, University of Michigan, Ann Arbor, MI 48109, USA

7 ²Department of Physics and Astronomy, West Virginia University, Morgantown, WV 26506, USA.

8 ³ KTH, Stockholm, Sweden.

9 ⁴ Los Alamos National Laboratory, Los Alamos, NM 87545, USA

10 **Key Points:**

- 11 • A one-hour long global simulation of Earth's magnetosphere with kinetic modeling
12 of the dayside reconnection
13 • Crater FTE is found at the early stage of a flux rope formation
14 • Kinetic phenomena are found from the global simulation

This is the author manuscript accepted for publication and has undergone full peer review but has not been through the copyediting, typesetting, pagination and proofreading process, which may lead to differences between this version and the [Version of Record](#). Please cite this article as doi: [10.1002/2017JA024186](https://doi.org/10.1002/2017JA024186)

Corresponding author: Yuxi Chen, yuxichen@umich.edu

Abstract

We perform a three-dimensional (3D) global simulation of Earth's magnetosphere with kinetic reconnection physics to study the flux transfer events (FTEs) and dayside magnetic reconnection with the recently developed magnetohydrodynamics with embedded particle-in-cell model (MHD-EPIC). During the one-hour long simulation, the FTEs are generated quasi-periodically near the subsolar point and move toward the poles. We find the magnetic field signature of FTEs at their early formation stage is similar to a 'crater FTE', which is characterized by a magnetic field strength dip at the FTE center. After the FTE core field grows to a significant value, it becomes an FTE with typical flux rope structure. When an FTE moves across the cusp, reconnection between the FTE field lines and the cusp field lines can dissipate the FTE. The kinetic features are also captured by our model. A crescent electron phase space distribution is found near the reconnection site. A similar distribution is found for ions at the location where the Larmor electric field appears. The lower hybrid drift instability (LHDI) along the current sheet direction also arises at the interface of magnetosheath and magnetosphere plasma. The LHDI electric field is about 8 mV/m and its dominant wavelength relative to the electron gyroradius agrees reasonably with MMS observations.

1 Introduction

Magnetic reconnection between the interplanetary magnetic field (IMF) and Earth's intrinsic dipole field is regarded as the most important mechanism for mass and energy transfer from the solar wind to the magnetosphere. Flux transfer events (FTEs) are widely considered as a phenomenon related to dayside non-steady reconnection [Russell and Elphic, 1978]. An FTE is a bundle of reconnected magnetic fluxtubes created at the magnetopause and moving anti-sunward along the magnetopause. Such events are characterized by a bipolar variation of the magnetopause normal magnetic field B_N , and are usually associated with an enhancement of core field, the magnetic field component along the axial direction of the FTE. An FTE exhibits a flux-rope structure in three-dimensional space. It has been observed that the plasma inside an FTE is usually a mixture of magnetospheric and magnetosheath plasma [Daly et al., 1981], indicating that FTEs are generated by magnetic reconnection process. The diameter of an FTE can vary from several ion inertial lengths [Eastwood et al., 2016] (a few hundred kilometers) to several Earth radii [Rijnbeek et al., 1984; Hasegawa et al., 2006]. In the dawn-dusk direction along the magne-

47 toopause, FTEs can extend over a long distance [Fear *et al.*, 2008]. FTEs frequently occur
48 as a quasi-periodic process, and Rijnbeek *et al.* [1984] reported that the FTEs were ob-
49 served about every 8 minutes during periods of southward magnetosheath magnetic field.

50 FTEs have been studied with various global numerical models. Compared to local
51 simulations, a global model can offer more realistic plasma and magnetic field context.
52 Fedder *et al.* [2002] used a global ideal MHD model to study the generation of FTEs. The
53 typical magnetic field signature is captured by their model, and their simulation suggests
54 that the FTEs are formed by non-steady reconnection along the separator at the mag-
55 netopause. Raeder [2006] performed a high resolution ideal MHD simulation with the
56 OpenGGCM model. FTEs formed by multiple X line reconnection [Lee and Fu, 1985]
57 with a tilted dipole field in this study. Dorelli and Bhattacharjee [2009] revisited the FTE
58 generation mechanism with resistive MHD using the OpenGGCM model, and the authors
59 argue that the FTEs are generated by flow vortices and the formation of new X lines is the
60 consequence, rather than the cause of FTE formation. Sibeck *et al.* [2008] studied crater
61 FTEs with the BATS-R-US MHD model. All these global simulations are based on ideal
62 or resistive MHD codes, and the generation of FTEs relies either on ad hoc resistivity
63 [Dorelli and Bhattacharjee, 2009] or numerical resistivity [Fedder *et al.*, 2002; Raeder,
64 2006]. Recently, a 2D-3V global magnetospheric hybrid-Vlasov simulation was performed
65 to study magnetopause reconnection and FTEs by Hoilijoki *et al.* [2017].

66 Typical FTEs are associated with an enhancement of the field strength at the center
67 of a flux rope. On the other hand, the so-called crater FTEs show more complicated struc-
68 ture: the center field is surrounded by two ‘trenches’ and the field strength usually show
69 a dip just at the center [LaBelle *et al.*, 1987; Owen *et al.*, 2008]. Typical FTEs are more
70 frequently observed than crater FTEs [Zhang *et al.*, 2010]. The generation mechanism of
71 crater FTEs has been explored with both numerical simulations [Sibeck *et al.*, 2008] and
72 analytic models [Zhang *et al.*, 2010]. Zhang *et al.* [2010] proposed that crater FTEs are the
73 initial stage of typical FTEs based on hundreds of events selected from THEMIS observa-
74 tions. The structure of the core field can be even more complicated, for example, Eriksson
75 *et al.* [2016] found a tripolar core field flux rope at the magnetopause.

76 It is widely accepted that the formation of FTEs is related to the dayside magne-
77 topause reconnection, which is a kinetic process for collisionless plasma. Therefore it is
78 important to include proper kinetic effects into the numerical model in order to produce
79 FTEs in a physical way. The MHD with embedded PIC (MHD-EPIC) model developed

80 by *Daldorff et al.* [2014] makes it feasible for the first time to use a kinetic model to study
81 reconnection and FTEs with realistic magnetospheric configuration. Because of the small
82 kinetic scales inside the magnetosheath, for example, the ion inertial length d_i is about
83 $60\text{km} \sim 1/100 R_E$, we have to artificially increase the kinetic scales in the present 3D
84 global simulation. As shown by our companion paper [*Tóth et al.*, 2017, submitted paper],
85 this scaling has no significant effect on the large scale structures, while the kinetic phe-
86 nomena occur at linearly increased scale. Since the kinetic scale physics is included in our
87 global model, the reconnection related kinetic phenomena, like the crescent shape electron
88 phase space distribution, the Larmor electric field and the lower hybrid drift instability
89 (LHDI), are all captured by the model. The crescent distribution was first found by *Hesse*
90 *et al.* [2014] from 2D local simulation, then observed by the Magnetospheric Multiscale
91 (MMS) mission recently [*Burch et al.*, 2016]. It is formed by the magnetosheath electrons
92 reaching the stagnation point and accelerated by the Hall electric field [*Bessho et al.*, 2016;
93 *Shay et al.*, 2016]. Recently, the origin of the crescent distribution is discussed by *Lapenta*
94 *et al.* [2017] with a high-resolution multiscale simulation. This special distribution has
95 been proposed as an indicator of the magnetic reconnection location [*Hesse et al.*, 2014].
96 The Larmor electric field is potentially another signature that can help to identify the lo-
97 cation of reconnection site [*Malakit et al.*, 2013]. It is on the magnetosphere side, normal
98 to the current sheet and pointing away from the X line. The lower hybrid drift instability
99 (LHDI) develops along the current direction [*Daughton*, 2003; *Roytershteyn et al.*, 2012],
100 and it has been observed recently by MMS satellites [*Graham et al.*, 2016]. LHDI was
101 considered as a potential source to create anomalous resistivity for reconnection [*Huba*
102 *et al.*, 1977], but previous research [*Mozzer et al.*, 2011] has suggested the related resistivity
103 may be not large enough. However a recent 3D simulation showed LHDI may still play an
104 important role near the diffusion region because of the presence of turbulence [*Price et al.*,
105 2016] .

106 In the following sections we will describe the MHD-EPIC model, the simulation
107 setup, and then discuss the simulation results.

108 2 Model description

109 The MHD-EPIC model has been successfully applied to investigate the interaction
110 between the Jovian wind and Ganymede's magnetosphere, where the ion inertial length is
111 large compared to the size of its magnetosphere [*Tóth et al.*, 2016]. In this paper, the same

112 model is applied to study Earth's magnetosphere, which is more challenging because of
 113 the small kinetic scale. The MHD-EPIC model two-way couples the BATS-R-US [Powell
 114 *et al.*, 1999; Tóth *et al.*, 2008] MHD code and the implicit particle-in-cell code iPIC3D
 115 [Markidis *et al.*, 2010] through the Space Weather Modeling Framework (SWMF) [Tóth
 116 *et al.*, 2005, 2012]. A general description of the these models and the simulation setup is
 117 provided in this session.

118 2.1 Global MHD model: BATS-R-US

119 In order to make the MHD model as complete as possible, the Hall term and the
 120 electron pressure gradient term are included in the generalized Ohm's law, and a separate
 121 electron pressure equation is solved. The generalized Ohm's law we use is:

$$122 \mathbf{E} = -\mathbf{u} \times \mathbf{B} + \frac{\mathbf{J} \times \mathbf{B}}{q_e n_e} - \frac{\nabla p_e}{q_e n_e} \quad (1)$$

123 where q_e , n_e and p_e are the charge per electron, electron number density and electron
 124 pressure, respectively. The electron pressure is obtained from:

$$125 \frac{\partial p_e}{\partial t} + \nabla \cdot (p_e \mathbf{u}_e) = (\gamma - 1)(-p_e \nabla \cdot \mathbf{u}_e) \quad (2)$$

126 where $\gamma = 5/3$ is the adiabatic index, and $\mathbf{u}_e = \mathbf{u} - \mathbf{J}/(q_e n_e)$ is the electron velocity.

127 From the numerical perspective, it is not trivial to incorporate the Hall term into
 128 the MHD equations. The Hall MHD equations support the whistler mode wave, which is
 129 dispersive and the characteristic speed is inversely proportional to the wavelength. Since
 130 the shortest wavelength that can be resolved in a numerical system is twice the cell size,
 131 the fastest whistler wave speed is proportional to $1/\Delta x$. For an explicit time integration
 132 scheme, the time step is limited by the CFL condition, which leads to a time step approx-
 133 imately proportional to $1/(\Delta x)^2$ for Hall MHD. In order to use a reasonably large time
 134 step, a semi-implicit time discretization is employed [Tóth *et al.*, 2012]. The semi-implicit
 135 scheme treats the stiff terms, which is the Hall term here, and other terms separately. Ex-
 136 cluding the Hall term, the rest of the equations are updated with an explicit scheme, and
 137 the time step is only limited by the fast magnetosonic wave speed. The Hall term is han-
 138 dled by an implicit solver after the explicit update has been done.

139 The typical solar wind condition at 1AU with purely southward IMF is used as
 140 the boundary condition to drive the magnetosphere: $\mathbf{B} = (0, 0, -5)$ nT, mass density
 141 $\rho = 5$ amu/cm³, ion pressure $p_i = 3.45 \times 10^{-3}$ nPa, and solar wind velocity $\mathbf{u} = (-400, 0, 0)$
 142 km/s. Electron pressure $p_e = 8p_i = 2.76 \times 10^{-2}$ nPa is used, so that after crossing

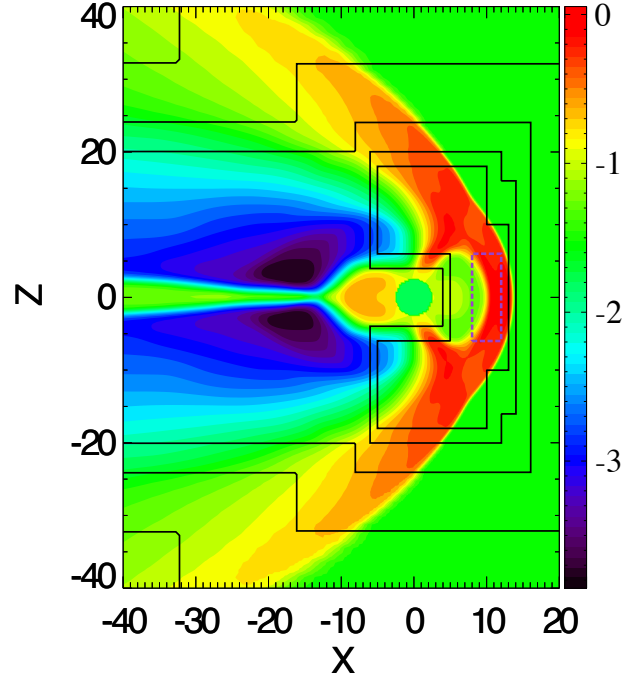
143 the shock, where the ions are heated by converting bulk into thermal energy while the
 144 electron thermal energy changes adiabatically, the ion-electron pressure ratio is about
 145 $p_i/p_e \sim 2.5$. Wang *et al.* [2012] shows that the temperature ratio T_i/T_e in the solar wind
 146 varies from $0.1 \sim 2$, and the ratio is about $4 \sim 12$ inside the magnetosheath. The T_i/T_e
 147 ratio, which is the same as p_i/p_e , used in the simulation is close to but slightly smaller
 148 than the typical observed ratio. We use $T_i/T_e = 1/8$, because our numerical experiments
 149 show that the electrons can be numerically heated in the PIC code if colder solar wind
 150 electrons are used for the upstream boundary condition. A magnetic dipole with 30116
 151 nT field strength at the Earth magnetic equatorial surface is used. Its magnetic axis is
 152 aligned with the z axis. The total magnetic field \mathbf{B} is split into the intrinsic dipole field
 153 \mathbf{B}_0 and the deviation \mathbf{B}_1 . A three-dimensional block-adaptive Cartesian grid is used to
 154 cover the whole magnetosphere: $-224 R_E < x < 32 R_E$, $-128 R_E < y < 128 R_E$ and
 155 $-128 R_E < z < 128 R_E$. Since we focus on the dayside dynamics in this paper, the mesh
 156 along the dayside magnetopause is refined to high resolution with $\Delta x = 1/16 R_E$ (see Fig-
 157 ure 1). 59 million cells are used in total. At the inner boundary $r = 2.5 R_E$, the density is
 158 fixed as 28 amu/cm^3 , the pressure and the magnetic field \mathbf{B}_1 have zero gradient, the radial
 159 velocity is zero, while the tangential velocity is calculated from the ionosphere electrody-
 160 namics model developed by Ridley *et al.* [2004].

166 2.2 Implicit particle-in-cell model: iPIC3D

167 The semi-implicit particle-in-cell code iPIC3D was developed by Markidis *et al.*
 168 [2010]. The advantage of iPIC3D over explicit particle-in-cell codes is that iPIC3D is lin-
 169 early unconditionally stable, so that iPIC3D can handle larger time step and larger cell size
 170 than explicit PIC codes. Compared to the explicit PIC method, the cell size of iPIC3D
 171 is chosen based on the scale of interest instead of the Debye length, and the time step of
 172 iPIC3D is not limited by the plasma frequency or the speed of light, but the accuracy con-
 173 dition, which requires $v_{rms}\Delta t/\Delta x < 1$ on all grid nodes for all species, where v_{rms} is the
 174 root mean square of macro-particle velocities. In order to make the simulation as efficient
 175 as possible while keeping the accuracy condition satisfied, we implemented an adaptive
 176 time step scheme:

$$177 \quad \Delta t = c_0 \cdot \min(\Delta x/v_{rms}, \Delta y/v_{rms}, \Delta z/v_{rms}), \quad (3)$$

178 which is calculated for each grid node and the minimum is taken over the whole PIC
 179 mesh. The root mean square velocity v_{rms} is similar to the thermal velocity but contains



161 **Figure 1.** Part of the meridional plane with the adaptive MHD grid and the PIC region. The color repre-
 162 sents the plasma pressure on a logarithmic scale. The black lines represent the refinement level, where the cell
 163 size changes. The resolution of the finest level around the dayside magnetopause is $1/16 R_E$, and the refine-
 164 ment ratio between two nearby levels is 2. The dashed magenta box ($8 R_E < x < 12 R_E$, $-6 R_E < z < 6 R_E$)
 165 is the edge of the PIC region covered by iPIC3D, and it extends from $-6 R_E$ to $6 R_E$ in the y direction.

180 the effect of bulk velocity. c_0 is a coefficient that should be smaller than 1. $c_0 = 0.4$ is
 181 used for the simulation in this paper.

182 Since the focus of this paper is the dayside magnetopause reconnection, the embed-
 183 ded PIC box is placed near the sub-solar magnetopause, where reconnection happens un-
 184 der purely southward IMF. In the GSM coordinates, the region inside $8 R_E < x < 12 R_E$
 185 and $-6 R_E < y, z < 6 R_E$ (see Figure 1) is solved by iPIC3D. The PIC region covers the
 186 magnetopause and it is just inside the bow shock. The size of the ion diffusion region is
 187 the same order as the ion inertial length, and this kinetic scale should be resolved in or-
 188 der to capture reconnection kinetic physics. However, the ion inertial length $d_i = c/\omega_{pi}$ is
 189 about $60\text{km} \sim 1/100 R_E$ for a typical magnetosheath density of $20 \text{amu}/\text{cm}^3$. This length
 190 is so small that it is extremely difficult to resolve even for a 3D global MHD model, not
 191 to mention the PIC code. Scaling up the kinetic length helps to reduce the required com-
 192 putational resources. In the present simulation, all the fluid values, including density, pres-

193 sure, velocity, IMF and dipole field strength, and also the derived values like the sound
194 speed, Alfvén velocity and plasma beta, are realistic so that the global structure of the
195 magnetosphere is comparable to the real system. On the other hand, the ion inertial length
196 is scaled up 16 times to about $1/6 R_E$ in the magnetosheath by artificially increasing ion
197 mass per charge by a scaling factor of 16. Since all the quantities are normalized in the
198 numerical model, there are several ways to understand or interpret the scaling. One way
199 is treating the scaling as changing the charge of ions and electrons. Compared with the
200 original system, we reduce the charge by a factor of 16 while all the other basic physical
201 quantities, like mass per ion, number density, and temperature remain realistic. From the
202 perspective of ideal magnetohydrodynamics, the scaled system is exactly equivalent to the
203 original one. For a particle-in-cell code, the reduction of charge per ion reduces the elec-
204 tromagnetic force on an ion and therefore increases the gyroradius and gyroperiod by a
205 factor of 16. But the gyroradius and the gyroperiod are still several orders smaller than
206 the global spatial and temporal scale, for example the distance from Earth to the magne-
207 topause and the time for the plasma moving from the subsolar point to the cusp, respec-
208 tively. How the scaling changes the structure of reconnection is discussed in detail in our
209 companion paper by *Tóth et al.* [2017, submitted paper]. We also apply a reduced ion-
210 electron mass ratio $m_i/m_e = 100$, which is sufficiently large to separate the electron and
211 ion scales. We choose $\Delta x = 1/32 R_E$ as the PIC grid resolution so that $d_i/\Delta x \sim 5$ and
212 $d_e/\Delta x \sim 0.5$. This resolution keeps a balance between the computational cost and the re-
213 quirement of resolving kinetic scales. 216 particles per cell per species are used and there
214 are about 9 billion particles in total inside the domain initially. Our numerical experiments
215 suggest smoothing the electric field \mathbf{E} and the current density \mathbf{j} can help to suppress the
216 numerical noise [*Tóth et al.*, 2017, submitted paper].

217 The typical magnetic field strength in the magnetosheath is about 30 nT, and the cor-
218 responding ion gyro-frequency is $\Omega_{ci} = 0.0286\text{Hz}$ and $\Omega_{ce} = 2.86\text{Hz}$ with scaled charge-
219 mass ratio. As mentioned above, the time step of iPIC3D is determined by the accuracy
220 condition (Eq. 3). From the simulation, we find the maximum thermal speed of electrons
221 inside the PIC domain is about 2500km/s, which leads to a time step of $\Delta t \sim 0.03s \sim$
222 $10^{-3}\Omega_{ci}^{-1} \sim 0.1\Omega_{ce}^{-1}$ with cell size $\Delta x = 1/32 R_E$. Therefore, the time step is small enough
223 to resolve the gyro-motion of both electrons and ions.

2.3 Coupling between BATS-R-US and iPIC3D

BATS-R-US and iPIC3D are coupled through the Space Weather Modeling Framework (SWMF). These two models are compiled together to generate a single executable file. Both models can run simultaneously on specified processors and the information exchange is parallelized and handled by the Message Passing Interface (MPI). The details of the two-way coupling has been described by *Daldorff et al.* [2014].

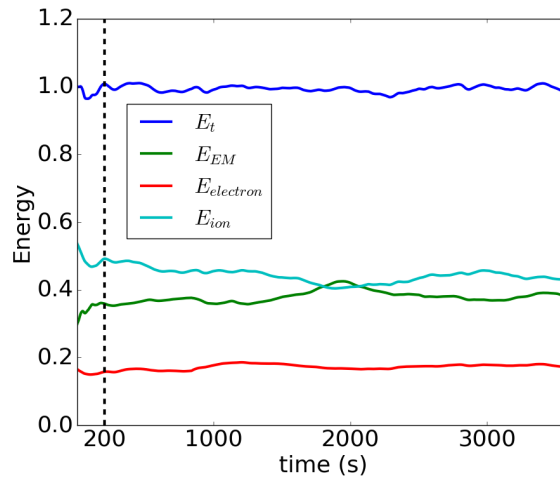
In the simulation presented in this paper, we run the Hall MHD code first with the local time stepping scheme to reach a steady state. Then BATS-R-US sends the information, including density, velocity, pressure and magnetic field, to iPIC3D. iPIC3D initializes the electric field based on the Ohm's law. The Maxwellian distributed particles are generated according to the fluid information so that iPIC3D and BATS-R-US have consistent density, velocity and pressure at the same position. After the PIC initialization, the MHD and PIC models update independently with their own time steps. The coupling frequency between these two models can be set to a value that is independent of the MHD or PIC time step. During the coupling, iPIC3D calculates moments of the particle distribution function, such as the density, velocity and pressure, and overwrites the MHD cells overlapping the PIC region. In return the MHD model provides electromagnetic field as well as particle boundary conditions for iPIC3D. For the particle boundary, iPIC3D removes the particles in the boundary cells, and re-generates new particles based on the fluid variables obtained from MHD. Between the two coupling time points, iPIC3D uses the latest information obtained from BATS-R-US as a boundary condition during each iteration. In the simulation presented here, the time step for BATS-R-US and iPIC3D are around $\Delta t_{MHD} = 0.015$ s and $\Delta t_{PIC} = 0.032$ s, respectively. The MHD code and the PIC code are coupled every time step. The time step of PIC is larger than that of MHD because the MHD time step is limited near the magnetic poles due to the high Alfvén speed, while these regions are outside the PIC domain.

Previously we generated particles in only one ghost cell layer [*Daldorff et al.*, 2014] as a particle boundary condition. Our numerical experiments suggested that using more layers (5 layers specifically in this paper) as the particle boundary, while the electromagnetic field boundary is still only enforced at the outermost layer, is helpful to smoothly transit from PIC to MHD. The MHD cells overlapped with the PIC particle boundary are not overwritten by PIC. A similar technique has been used to implement open boundary condition for stand-alone PIC simulations [*Peng et al.*, 2015].

257 We run the simulation on 6400 processors for 170 hours on Blue Water supercom-
 258 puter [Bode *et al.*, 2012] to model one hour of simulation time. iPIC3D and BATS-R-US
 259 use about 80% and 15% of the simulation time, respectively. The coupling and other over-
 260 head use the remaining 5%.

261 2.4 Energy conservation

262 Even though the PIC region is not a closed system, therefore mass and energy flow
 263 into and out of the region, it is still important to check the energy variation during the
 264 simulation to make sure the PIC model does not suffer from numerical heating or cool-
 265 ing. The normalized energy changes are shown in Figure 2. Throughout the simulation,
 266 the total energy E_t variation is less than 3%. The small variation suggests that the numer-
 267 ical heating or cooling are insignificant. The initial condition for iPIC3D is under MHD
 268 equilibrium, but not necessarily under Vlasov equilibrium. The electromagnetic field en-
 269 ergy E_{EM} and kinetic energy of each species normalized by the initial total energy are
 270 also shown in Figure 2. During the first several minutes, energy is transferred from the
 271 particles to the electromagnetic field. After 200s, the ion and electron energy decreases
 272 about 5%, while the electromagnetic field energy increases from 0.3 to about 0.36. This is
 273 the transition from the MHD steady state to a PIC preferred state. Further change of these
 274 energies are gradual and small. E_{EM} is mainly magnetic field energy, which is about 3
 275 orders larger than the electric field energy.



276 **Figure 2.** The normalized the total energy E_t , electric field and magnetic field energy E_{EM} , ion energy
 277 E_{ion} and electron energy $E_{electron}$. They are normalized by the initial total energy.

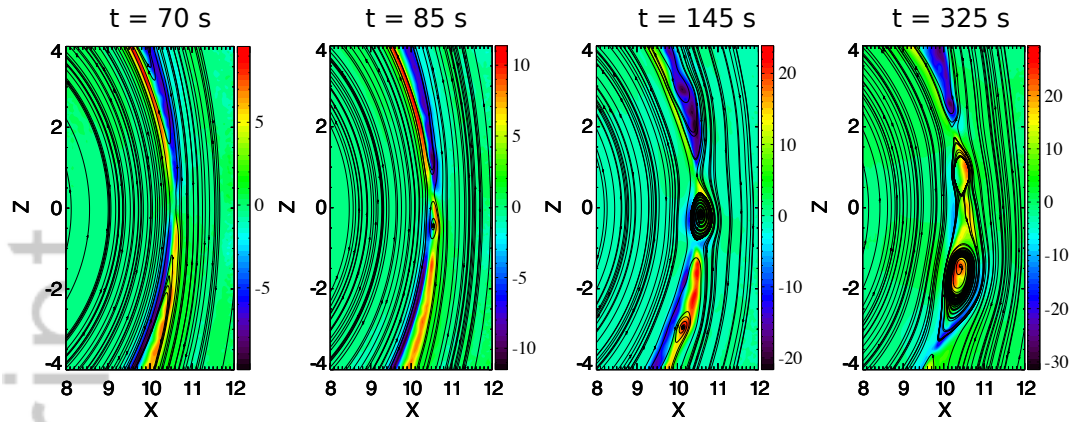
3 Results

3.1 Overview

The iPIC3D code is initialized from a steady Hall MHD state, which is shown in Figure 1. The steady state is obtained from the Hall MHD run by using a local time stepping scheme, and a reconnection X line already exists near the equatorial plane along the dayside magnetopause. Since the local time stepping scheme is diffusive in this case, the reconnection signature near the X line is weak, for example, the Hall magnetic field strength is only about 1 nT. The PIC code inherits the magnetic field topology and starts evolving based on Maxwell's equations and the motion of the macro-particles. An overview of the evolution of the dayside magnetopause is shown in Figure 3, which contains the Hall magnetic field B_y and the field lines at the meridional plane inside the PIC box. At $t = 70$ s, B_y has already increased to about 8 nT. The Hall field extends far away from the X line with roughly the same field strength for each branch. 15s later, south of the existing reconnection point, another X line starts to form at around $x = 10.2 R_E$ and $z = -1 R_E$. At $t = 145$ s, both X lines can be seen clearly, and a flux rope like structure forms between the two X lines. The top X line has moved to about $z = 0.5$. The bottom X line is almost steady to this point, but it will move southward later. At $t = 325$ s, the top and bottom X lines reach about $z = 1.8$ and $z = -3.5$, respectively, and the center of the flux rope is moving southward with the bottom X line. Since the flux rope is moving away from the top X line, the current sheet between them becomes unstable and a secondary flux rope is generated (rightmost panel of Figure 3). During the one hour simulation, flux ropes form near the subsolar point and move toward the poles quasi-periodically. More details about the reconnection and the flux ropes, for both macroscopic and microscopic scales, are discussed in the following sub-sections.

3.2 Evolution of FTEs

More complicated structures arise in 3D. Flux ropes colored with the ion velocity z component u_{iz} at different times are shown in Figure 4. At $t = 100$ s, a short flux rope appears near the subsolar point. It is labeled as FTE-A. This flux rope extends from $y \sim -1 R_E$ to $y \sim 1 R_E$ in the dawn-dusk direction. It suggests that next to the primary X line near $z = 0$, another X line starts to form south of the subsolar point. We have checked a series of 2D $x - z$ plane cuts, and found that the signature of reconnection, like the ion jets, at the second X line is clear at $y = 0$, but appears very weak far away from the Sun-



302 **Figure 3.** A series of snapshots showing B_y strength (color) and the projected magnetic field lines in the
 303 meridional plane inside the PIC region. The color bar is different in each plot.

312 Earth line, for example at $y = 0.78 R_E$ or $y = -0.78 R_E$. At $t = 150$ s, the flux rope has
 313 extended significantly in both dawn and dusk directions. Along the flux rope, the ion ve-
 314 locity varies. Close to the dusk side (positive y), the flux rope moves slowly, because the
 315 northward reconnection jet produced by the second X line slows down the southward flow
 316 originating from the primary X line. Close to the dawn side (negative y), the flux rope
 317 moves faster, because the reconnection at the second X line is not strong enough to sig-
 318 nificantly slow the southward flow ejected from the primary X line. The variation of the
 319 z component of the ion velocity along the flux rope, which is approximately aligned with
 320 the y direction, makes the flux rope inclined. At $t = 240$ s, the flux rope is even more
 321 tilted because of the varying ambient ion jet velocity. A new small flux rope, FTE-B in
 322 Figure 4, is generated at $t = 320$ s above FTE-A. FTE-A bifurcates at $y \sim -2.5$ and the
 323 new branch extends along the dawn-northward direction. FTE-A keeps moving southward
 324 while FTE-B is growing. At $t = 540$ s, a large portion of FTE-A, except for the dawn
 325 part, has already moved to the southern edge of the PIC domain ($z = -6$). FTE-B elon-
 326 gates significantly along the dawn-dusk direction. It is twisted at the dawn side so that
 327 the axial direction is almost parallel to the z -axis. At the dusk side, FTE-B connects to a
 328 newly formed flux rope FTE-C. At $t = 660$ s, FTE-B and FTE-C have merged and become
 329 indistinguishable. These 3D plots suggest: 1) flux ropes arise from multiple X line recon-
 330 nection and can grow in time along the dawn-dusk direction, 2) the pole-ward moving
 331 velocity varies along a flux rope and makes them tilted, and 3) two flux ropes can merge
 332 and form a new long flux rope.

333 Since the PIC code is two-way coupled with the MHD model, the flux ropes can
 334 smoothly move out of the PIC region. Figure 5 shows a series of snapshots of j_y and field
 335 lines of FTE-A in the meridional plane (x - z plane) after it leaves the PIC domain. FTE-A
 336 moves southward along the magnetopause after being generated near the subsolar point.
 337 At $t = 600$ s, the flux rope is already close to the southern cusp. There is strong axial
 338 current $j_y \sim 0.02 \mu\text{A}/\text{m}^2$ near the center of the flux rope. As FTE-A moves toward the
 339 cusp, j_y inside the flux rope decreases in intensity, which indicates the dissipation of the
 340 magnetic helicity, as we can see at $t = 660$ s. When the FTE reaches the center of the
 341 cusp ($t = 720$ s), the field lines at the leading edge of the FTE and the cusp field lines are
 342 anti-parallel and create a narrow and short current sheet with negative j_y around $x \sim 4 R_E$
 343 and $z \sim -9.5 R_E$. The ion velocity u_{iz} at $x = 4 R_E$ in Figure 6 shows a jump around
 344 $z = -9.5 R_E$. The narrow current sheet and the velocity jump imply that reconnection oc-
 345 curs between the flux rope field lines and the cusp field lines. At $t = 840$ s, after FTE-A
 346 leaves the cusp, the signature of the flux rope becomes very weak: even though the mag-
 347 netic field is still perturbed, the j_y component is close to zero near the center and no ‘O’
 348 line can be found. Finally, the remnant of the flux rope completely disappears as it moves
 349 toward the tail. Beside the FTE presented here, all other FTEs are also dissipated near
 350 the cusps in the meridional plane. Since an FTE is a 3D structure, its behavior far
 351 from the meridional plane needs to be further explored. FTEs were observed by the satel-
 352 lite along the distant tail magnetopause ($x = -67 R_E$) on the dusk flank [Eastwood *et al.*,
 353 2012]. One possibility to explain the conflict between the simulation and the observation
 354 is that these FTEs may bypass the cusps and move along the flank from the dayside to the
 355 tail magnetopause.

3.3 Magnetic field signature

363
 364 Since the most widely used indicator of FTEs in satellite data is the magnetic field
 365 signature, we discuss how the flux rope magnetic field looks like along a virtual satel-
 366 lite trajectory. A series of meridional cuts are shown in Figure 7 to illustrate the mag-
 367 netic field evolution. At $t = 290$ s, north of the FTE-A event, there is an X line at about
 368 $z = 1 R_E$ surrounded by the quadrupolar Hall magnetic field B_y . As expected, the two
 369 branches on the magnetosheath side with amplitude of ~ 30 nT are stronger than the other
 370 two on the magnetosphere side with amplitude of ~ 10 nT. Near the X line, the magne-
 371 tosheat and magnetosphere are separated by a current sheet with very weak magnetic

372 field. 30 s later, another X line near $z = 0$ arises, and an O line forms between the two
373 X lines. Around the edge of the O lines, the azimuthal component of the magnetic field
374 grows, while the B_y component is still very weak just near the center. We note that the
375 strong field on the magnetosheath side of the flux rope is mainly contributed by the B_z
376 component because of the accumulation of the inflow of magnetic flux. The recon-
377 nection at the northern X line is stronger than that of the southern one, so the ion jet around
378 the O line is moving southward with a slow speed less than 100 km/s. Inside the O line,
379 the pressure starts increasing. 100 s later, the pressure at the center of the flux rope has
380 reached about 1.3 nPa while the core field is still small. At $t = 540$ s, the O line struc-
381 ture continues to grow as the two X lines move northward and southward, respectively.
382 We can see the core field B_y at the center of the O line has grown to a significant value
383 of ~ 30 nT now, while the center pressure drops to ~ 1.0 nPa. The converging jets from
384 the two X lines are comparable and the flux rope is almost steady. 180 s later, the core
385 field grows to ~ 40 nT and the corresponding pressure drops to about 0.8 nPa. The whole
386 structure at this stage is moving northward driven by the ion jet generated by the south-
387 ern X line. To demonstrate the scaling factor has weak influence on the global structures,
388 we performed another simulation with ion inertial length increased by a factor of 32. The
389 simulation results are shown in Figure 8. The FTE in Figure 8 develops similarly to the
390 one in Figure 7: the core field grows gradually and the ion pressure is anti-correlated with
391 the core field strength. The FTEs in Figure 8 and Figure 7 also have comparable sizes.

392 At the early time when the O line just formed, for example, at $t = 420$ s, the weak
393 core field is surrounded by relatively large toroidal fields. We argue that this is an exam-
394 ple of the so-called ‘crater FTEs’ that have been observed by spacecrafts [LaBelle *et al.*,
395 1987; Zhang *et al.*, 2010]. Since the O line moves slowly during its initial stage of for-
396 mation, the magnetic field observed at a fixed point can not reflect its global structure.
397 Instead, the magnetic field along the magnetopause (the red curve in the left panel of Fig-
398 ure 9) is shown in the right panel of Figure 9 to illustrate its magnetic field structure.
399 Along the magnetopause, from south to north, the B_x field, which is roughly normal to
400 the magnetopause, reaches a local minimum of ~ -15 nT at $z = 0$ and then quickly in-
401 creases to ~ 15 nT at $z = 1 R_E$. The flux rope is bounded by the depressed magnetic
402 field ‘trenches’ at $z = -0.2 R_E$ and $z = 2 R_E$ as indicated by B_t . The depression re-
403 sults from the low magnetic field strength inside the current sheet as can be seen from
404 the right panel of Figure 9. B_t reaches a local maximum at the same position of the B_x

405 peaks ($z = 0 R_E$ and $z = 1 R_E$), while the field strength decreases to about 10 nT between
406 the peaks. We refer to the event on 30 July 2007 observed and analyzed by *Zhang et al.*
407 [2010] for comparison. Figure 6 of *Zhang et al.* [2010] shows the magnetic field signature
408 of this event. Even though the 30 July 2007 event has a large guide field (corresponding
409 to B_y component in our simulation), and its magnetic field around the flux rope is more
410 steady than our simulation, the whole structure of this event is similar to what is shown in
411 Figure 9.

412 As the flux rope evolves, the core field strength grows to a significant value. The
413 magnetic field measured at a fixed position $x = 10.2 R_E$, $z = 2.75 R_E$ is shown in the
414 right panel of Figure 10. The vertical dashed line at $t = 760$ s represents the location of
415 the maximum B_t . Around this time, the B_x field, which is roughly perpendicular to the
416 magnetopause, jumps from ~ 5 nT to ~ -20 nT within about 25 s. At $t = 760$ s, both the
417 axial field B_y and the total field B_t reach a maximum. These features match the signatures
418 of the FTE observed by *Zhang et al.* [2010]. During the one-hour long simulation, there
419 are ten FTEs with significant core field moving across the southern PIC edge. The occur-
420 rence frequency is consistent with observations [*Rijnbeek et al.*, 1984] and previous MHD
421 simulations [*Raeder*, 2006].

422 The IMF is purely southward in our simulation and there is no uniform background
423 guide field at the magnetopause. But a significant core field can still arise during the
424 FTE generation and evolution as seen in Figure 7. When a flux rope is still close to the
425 X lines, the core field may be encompassed by the Hall magnetic field generated by the
426 reconnection, resulting in complicated guide field structure. The B_M field at $t = 540$ s is
427 shown in Figure 11. In order to compare with observations, the magnetic field has been
428 transformed into a boundary normal coordinate system (**LMN**), in which the **N** compo-
429 nent points outward, normal to the magnetopause, the **M** component is determined by
430 $\mathbf{N} \times \mathbf{Z}_{GSM}$ and the **L** component completes the right-hand coordinate system. Since the
431 plot is shown in the meridional plane, the \mathbf{Y}_{GSM} direction is anti-parallel to the **M** di-
432 rection. Around the flux rope center, the guide field B_M is negative, while the southern
433 part of this flux rope is surrounded by positive B_M . The polarity of the positive 'Y' shape
434 B_M is consistent with the Hall magnetic field generated by the X line at $z = -1 R_E$. If
435 a satellite is moving across the flux rope along the red solid line in the left panel of Fig-
436 ure 11, the satellite will observe a tripolar guide field structure (right panel of Figure 11).
437 Similar structure was first observed in the solar wind [*Eriksson et al.*, 2015], and it was

438 also observed by the Polar satellite at the magnetopause (see Figure 1 of *Eriksson et al.*
 439 [2016]). The Polar event shows a large negative B_M core field bounded by two narrow
 440 B_M depressions in the presence of a large background guide field. There is no background
 441 guide field in our simulation and thus the right panel of Figure 11 shows a pure tripolar
 442 structure: the large negative B_M field is surrounded by two relative small positive peaks.
 443 Despite the difference in the background guide field, the topology of B_M obtained from
 444 our simulation is very similar to the Polar observation.

460 3.4 Kinetic features

461 We have examined the global structure of the FTEs in the previous discussion. In
 462 this subsection, we will demonstrate that the underlying kinetic physics is properly cap-
 463 tured by our model. The Larmor electric field, identified by *Malakit et al.* [2013], is a lo-
 464 calized electric field that appears on the magnetospheric side of the dayside reconnection
 465 site. The x-component of the electric field E_x at the end of the simulation ($t=3600s$) is
 466 shown in Figure 12. The positive E_x pointing towards the Sun along the magnetopause
 467 is the Hall electric field, while behind the Hall electric field, the localized negative field
 468 pointing towards the Earth is the Larmor electric field. A 1D cut through the reconnect-
 469 tion site along the x direction is also shown in Figure 12. The Larmor field strength is -3
 470 mV/m, the magnetospheric side ambient field is about 2 mV/m, and the nearby Hall field
 471 is about 12 mV/m. These values are reasonably close to the MMS observation by *Graham*
 472 *et al.* [2016], for which the Hall electric field strength was ~ 20 mV/m and the Larmor
 473 field strength was about 10 mV/m (see Figure 2 of *Graham et al.* [2016]).

474 Even though the ion inertial length is scaled up by a factor of 16 in the present sim-
 475 ulation, the electric field strength is not sensitive to the scaling factor. Ignoring the elec-
 476 tron inertia term, the generalized Ohm's is:

$$\mathbf{E} = -\mathbf{u}_i \times \mathbf{B} + \frac{1}{q_i n_i} \mathbf{j} \times \mathbf{B} - \frac{1}{q_i n_i} \nabla p_e = -\mathbf{u}_e \times \mathbf{B} - \frac{1}{q_i n_i} \nabla p_e \quad (4)$$

477 *Tóth et al.* [2017, submitted paper] shows the electron velocity \mathbf{u}_e of the current sheet does
 478 not change with the scaling factor while the current sheet width scales. The gradient of
 479 electron pressure is inversely proportional to the scaling factor, because the pressure jump
 480 is fixed across the current sheet and the current sheet width is proportional to the scaling
 481 factor. Since the charge per ion or electron is also reduced by the same factor, the scaling
 482 does not change the electric field strength. Besides the scaling of the ion inertial length,
 483 a reduced ion-electron mass ratio $m_i/m_e = 100$ is used in this study to increase electron

484 kinetic scales (see section 2.2). The influence of the mass ratio m_i/m_e has been studied in
 485 numerous papers [Shay and Drake, 1998; Hesse et al., 1999; Ricci et al., 2004; Shay et al.,
 486 2007; Lapenta et al., 2010]. For the Larmor electric field, Malakit et al. [2013] specifi-
 487 cally estimates its amplitude to be:

$$E \sim \frac{k_B T_i}{q_i r_i} \quad (5)$$

488 where k_B is the Boltzmann's constant, T_i , q_i and r_i are the temperature, charge per ion
 489 and ion Larmor radius of the ions on the magnetospheric side. In the simulation, q_i is re-
 490 duced by a factor of 16 and r_i becomes 16 times larger compared to the realistic situation,
 491 while the temperature T_i does not change. So, the scaling of inertial length should not
 492 influence the strength of the Larmor electric field. On the magnetosheath side, our simula-
 493 tion shows the ion temperature is about 2×10^6 K, and the magnetic field strength is about
 494 60 nT. Substituting these values into Eq. 5 gives $E \sim 5.5$ nT. As mentioned above, the
 495 value obtained from simulation is about -3 mV/m.

496 The crescent shape electron phase space distribution has been observed near the
 497 electron diffusion region at the dayside magnetopause by MMS [Burch et al., 2016]. The
 498 same distribution is also found in our 3D global simulation. The phase space distribution
 499 of electrons inside a cube region: $10.27 R_E < x < 10.33 R_E$, $-0.3 R_E < y < 0.3 R_E$ and
 500 $-2.1 R_E < z < -1.9 R_E$ is shown in Figure 12. The crescent distribution is found in the
 501 $V_y - V_x$ plane, corresponding to the two velocity components perpendicular to the magnetic
 502 field. The crescent hot electrons are drifting along negative y direction with a speed close
 503 to 3000 km/s. The direction of the flow is consistent with the $\mathbf{E} \times \mathbf{B}$ direction, and the ve-
 504 locity of the crescent particles is very close to the MMS observation [Burch et al., 2016].
 505 Slightly further away from the reconnection site, where the Larmor field appears, inside a
 506 cube $10.08 R_E < x < 10.14 R_E$, $-0.3 R_E < y < 0.3 R_E$ and $-2.1 R_E < z < -1.9 R_E$,
 507 the ion phase space distribution also presents crescent like shape as it is shown in Fig-
 508 ure 12(c). The crescent ions drift in positive y direction because E_x is negative. We also
 509 checked the distributions for particles inside the current sheet but far from the reconnect-
 510 ion site, and no crescent distributions are found for either electrons or ions.

517 Kinetic effects along the magnetopause current direction are also captured by our
 518 3D MHD-EPIC model. Figure 13 shows the fully developed lower hybrid drift instabil-
 519 ity (LHDI) at the end of the simulation ($t=3600$ s) at the $z = -3 R_E$ plane. The electric
 520 field E_M shown in Figure 13 is the \mathbf{M} component in the boundary normal coordinates,
 521 and \mathbf{M} is anti-parallel to the current direction. The black curve in Figure 13 separates the

522 negative and positive B_z . We can see the LHDI appears along the magnetopause on the
 523 magnetospheric side. A closer view of E_M , as well as B_z , ion mass density ρ_i and elec-
 524 tron velocity u_{ey} are also shown Figure 13. The LHDI arises near the interface of magne-
 525 tosheath and magnetosphere, where there is a sharp density gradient. B_z , ρ_i and u_{ey} show
 526 sawtooth pattern at the same location. The amplitude of the LHDI electric field is about 8
 527 mV/m, which is consistent with MMS observations [Graham *et al.*, 2016]. The dominant
 528 wavelength shown in Figure 13(b) is about $0.38 R_E$, and the ambient magnetosheath side
 529 electron gyroradius is about $r_e = 0.025 R_E$ with the artificially changed charge per elec-
 530 tron mass ratio, which results in $kr_e \sim 0.4$, where $r_e = m_e v_e / (q_e B)$ and v_e is defined as
 531 $v_e = \sqrt{2T_e / m_e}$. The value of kr_e is also consistent with observations [Graham *et al.*, 2016]
 532 and theory [Daughton, 2003]. We analyzed the LHDI at different times and different loca-
 533 tions; the value of kr_e varied from ~ 0.3 to ~ 0.5 , and $kr_e \sim 0.4$ is a typical value. Sim-
 534 ilar to the argument above with the Ohm's law, the electric field strength is not sensitive
 535 to the scaling; that is why the LHDI electric field strength agrees with MMS observations.
 536 But the length scale does change with the scaling. The charge per mass of electron q_e / m_e
 537 is artificially increased by a factor of 294 in the simulation, and the electron thermal ve-
 538 locity is reduced by a factor of $\sqrt{18.36} = 4.3$ for $m_i / m_e = 100$. The magnetic field is
 539 realistic, hence the electron gyroradius is about 68 times larger than in reality. If we scale
 540 back the LHDI wavelength of the simulation by the same factor, it will be ~ 35 km. As a
 541 comparison, MMS observed 10km \sim 13km wavelength [Graham *et al.*, 2016]. Figure 13(f)
 542 shows the isosurfaces of $E_M = 4$ mV/m colored by the ion velocity u_{iz} viewed from the
 543 Sun. Along the magnetic field direction, the isosurfaces are cut off two or three times.
 544 The ion velocity jumps or even changes directions across a cut-off region. It suggests that
 545 these cut-off regions correspond to reconnection sites and that the LHDI electric field is
 546 weak near the diffusion regions [Pritchett, 2013].

553 3.5 Comparison with Hall MHD

554 For comparison, we also run a pure Hall MHD simulation with the same setup ex-
 555 cept the PIC region is removed and the MHD grid resolution around the dayside magne-
 556 topause is refined to $1/32 R_E$, which is the resolution used by PIC in the MHD-EPIC run.
 557 Even for Hall MHD, resolving the ion inertial length is necessary in order to capture the
 558 Hall effect correctly. Due to the small kinetic scale inside the magnetosheath, scaling the
 559 ion inertial length is also required for a global Hall MHD simulation since Hall MHD is

560 also computationally expensive as we will see. We note that the ion inertial length in the
561 pure Hall MHD simulation is also scaled up by a factor of 16 so it can be resolved with
562 the $1/32 R_E$ cell size. Hall MHD is reasonably optimized by using a semi-implicit scheme
563 to overcome the time step imposed by the whistler mode wave and speed up the simula-
564 tion. It still takes 6400 cores running about 67 hours to model one hour because of the
565 high resolution and the stiffness of the Hall term. As a comparison, the MHD-EPIC simu-
566 lation (170 hours on 6400 cores) is about 2.5 times more expensive. Hall MHD produces
567 the Hall magnetic field near the X line and generates flux ropes in a way similar to MHD-
568 EPIC. But Hall MHD cannot reproduce the kinetic features, neither the crescent particle
569 distributions nor the LHDI.

570 **4 Summary and conclusion**

571 We have performed a one-hour long high-resolution global simulation with the MHD-
572 EPIC model to study dayside reconnection and FTEs. Our simulation is the first attempt
573 to investigate the FTEs and reconnection with kinetic physics resolved in a realistic mag-
574 netopause environment. Although the kinetic scale is artificially increased to reduce the
575 computational cost, the model still captures the kinetic features very well. MMS observa-
576 tions, like the crescent particle phase space distribution and LHDI, are reproduced in our
577 model. The FTEs from the simulation also agree well with spacecraft observations. The
578 key results from the present simulation are:

- 579 • When an FTE arises, its cross section is small and it is short in the dawn-dusk di-
580 rection. During its growth, the cross section increases and the FTE extends along
581 the dawn-dusk direction.
- 582 • An FTE forms near the subsolar point and moves toward the poles under steady
583 southward IMF conditions. When the FTE reaches the cusp, reconnection happens
584 between the FTE magnetic field and the cusp magnetic field lines, thus dissipat-
585 ing the FTE. The signature of the FTE in the meridional plane is weak behind the
586 cusps.
- 587 • An FTE is flanked by two reconnection sites during its formation, and the converg-
588 ing ion jets are found around the FTE.
- 589 • The present simulation confirms that the 'crater FTEs' magnetic field signature can
590 be found at the early stage of an FTE formation when the axial magnetic field is

591 still weak. A strong core field may develop as the FTE evolves, and the Hall mag-
592 netic field may provide the initial seed core field. Therefore a fully developed FTE
593 has the typical strong core field structure.

- 594 • A tripolar guide field structure is found from our simulation.
- 595 • The Larmor electric field is found near the reconnection site on the magnetospheric
596 side, and its amplitude is about -3 mV/m.
- 597 • A crescent electron phase space distribution is found near the reconnection site
598 where the Hall electric field reaches its maximum. A similar distribution is also
599 found for ions at the place where the Larmor electric field appears.
- 600 • The lower hybrid drift instability (LHDI) appears at the interface of the magne-
601 tosheath plasma and magnetosphere plasma. The LHDI electric field peak strength
602 is about 8 mV/m, and a typical ratio between its wavelength and the electron gyro-
603 radius is about $kr_e \sim 0.4$. The simulation agrees with the MMS observations and
604 theory.

605 Compared to the models relying on ad hoc resistivity or numerical resistivity to gener-
606 ate FTEs or investigate reconnection process, our 3D MHD-EPIC model makes one sig-
607 nificant step forward by incorporating a self-consistent kinetic description of reconnection
608 into a global MHD model. While the kinetic scales are increased by artificially reduc-
609 ing the charge per mass for both ions and electrons, all the other parameters are realistic.
610 The scaling changes the size of kinetic features, for example the wavelength of LHDI, but
611 other values, like the strength of Larmor electric field or LHDI electric field, are not mod-
612 ified by the scaling. Another artificial change is the solar wind electron pressure. It is set
613 to a value 8 times larger than the ion pressure so that $p/p_e \sim 2.5$ inside the magnetosheath
614 while the ratio is usually about 4 ~ 12 from observation [Wang *et al.*, 2012]. The artifi-
615 cially increased electron pressure can help to stabilize the simulation, and it does not devi-
616 ate significantly from the observed values. We plan to improve this in the future studies.

617 The MHD-EPIC model offers a powerful tool to study magnetospheric physics. The
618 PIC code only covers the dayside magnetopause in the present simulation. As a natural
619 extension, it can be elongated to cover the bow shock so that the kinetic processes as-
620 sociated with the bow shock can be modeled. Another future application is covering the
621 tail reconnection site with another PIC region, so that both dayside and tail reconnections
622 are handled by a kinetic code. Then we will be able to study substorm in a more realis-
623 tic way. Both the ion pressure and electron pressure are solved by the MHD code in the

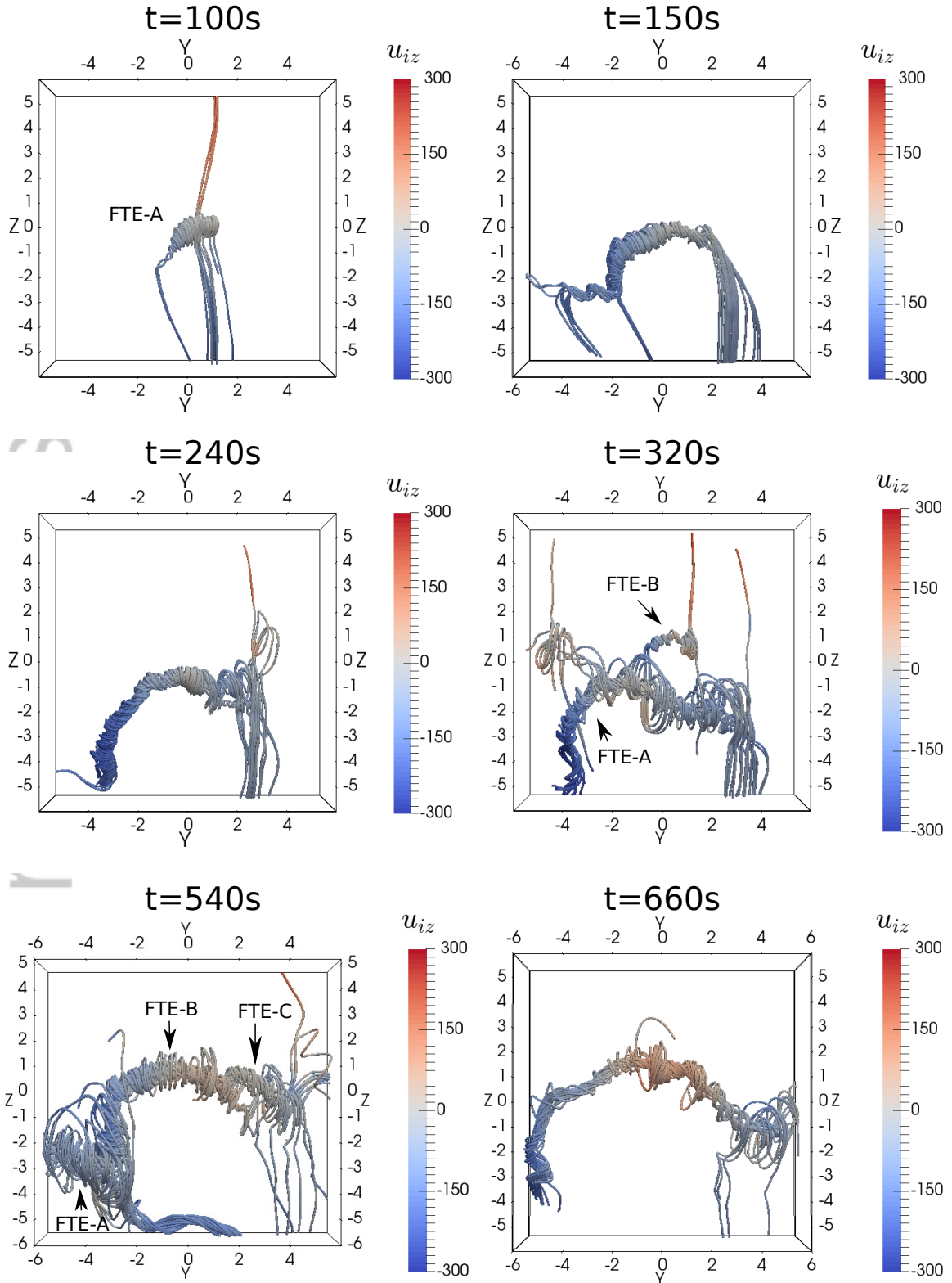
624 current simulation, but they are scalars. The missing of the off-diagonal pressure tensors
625 introduces discrepancy at the boundaries of the PIC code. This discrepancy can be im-
626 proved by using a ten-moment fluid model in the future.

627 **Acknowledgments**

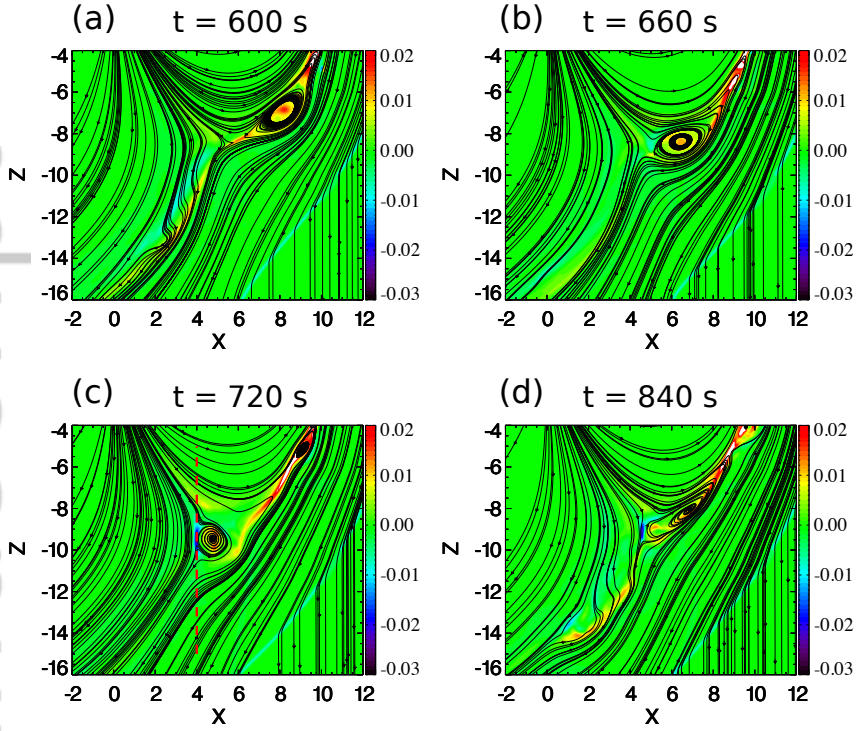
628 This work was supported by the INSPIRE NSF grant PHY-1513379, NSF strategic capa-
629 bility grant AGS-1322543, NASA grant NNX16AF75G, NASA grant NNX16AG76G, and
630 the Space Hazards Induced near Earth by Large, Dynamic Storms (SHIELDS), and the
631 Impacts of Extreme Space Weather Events on Power Grid Infrastructure projects funded
632 by the U.S. Department of Energy DE-AC52-06NA25396 through the Los Alamos Na-
633 tional Laboratory Directed Research and Development program.

634 Computational resources supporting this work were provided on the Blue Waters su-
635 per computer by the NSF PRAC grant ACI-1640510, on the Pleiades computer by NASA
636 High-End Computing (HEC) Program through the NASA Advanced Supercomputing
637 (NAS) Division at Ames Research Center, and from Yellowstone (ark:/85065/d7wd3xhc)
638 provided by NCAR's Computational and Information Systems Laboratory, sponsored by
639 the National Science Foundation.

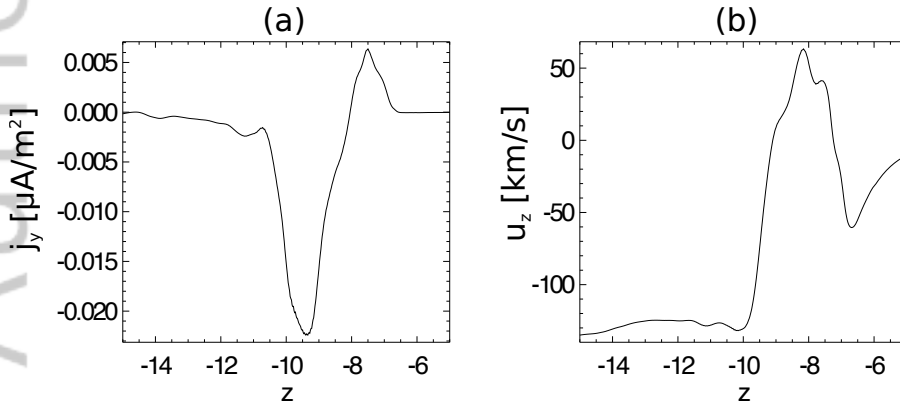
640 The SWMF code (including BATS-R-US and iPIC3D) is publicly available through
641 the csem.engin.umich.edu/tools/swmf web site after registration. The output of the simula-
642 tions presented in this paper can be obtained by contacting the first author Yuxi Chen.



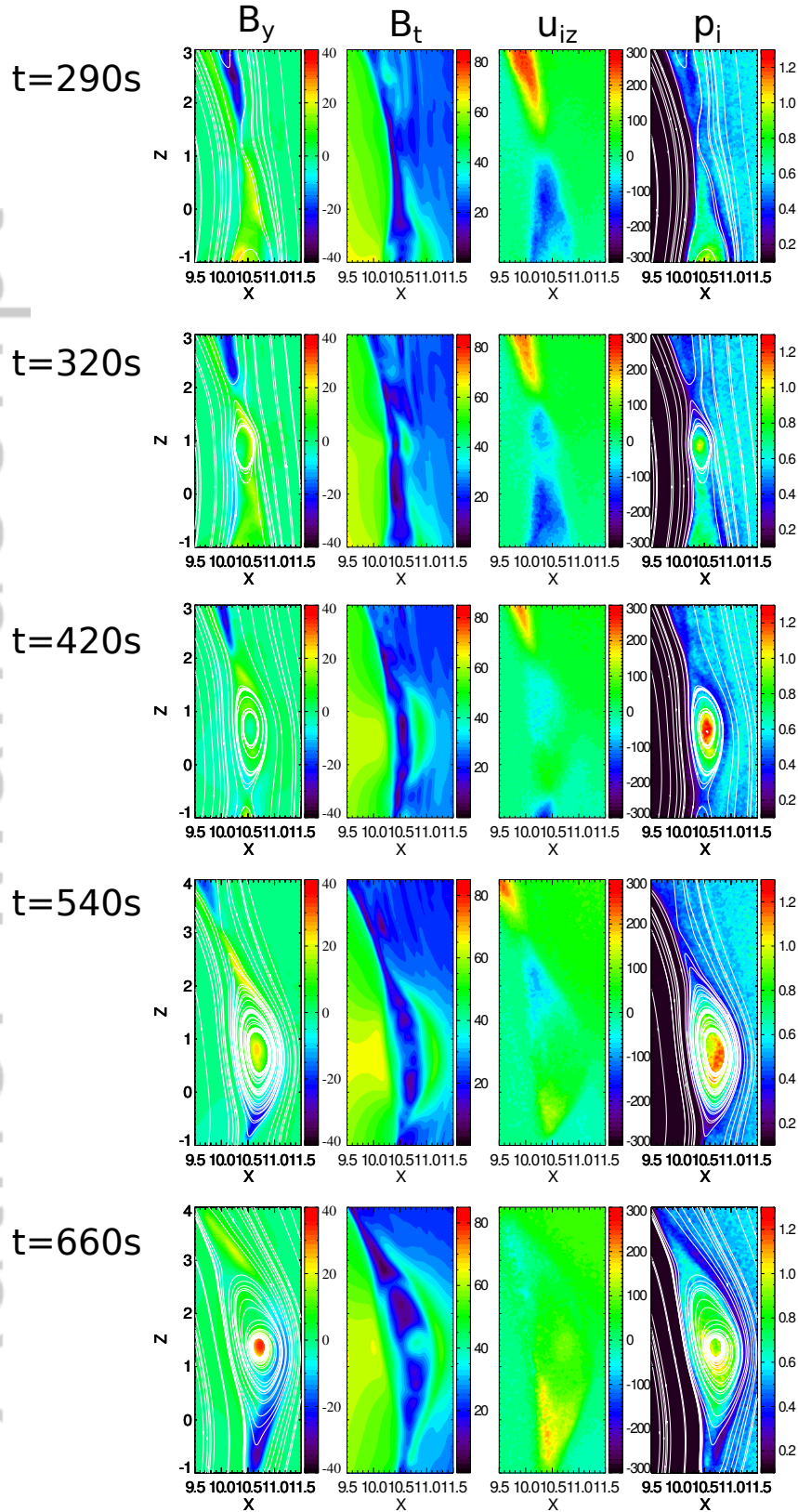
356 **Figure 4.** Evolution of FTEs. Viewed from the Sun, a series of snapshots are shown with magnetic field
 357 lines colored by ion velocity u_{iz} [km/s].



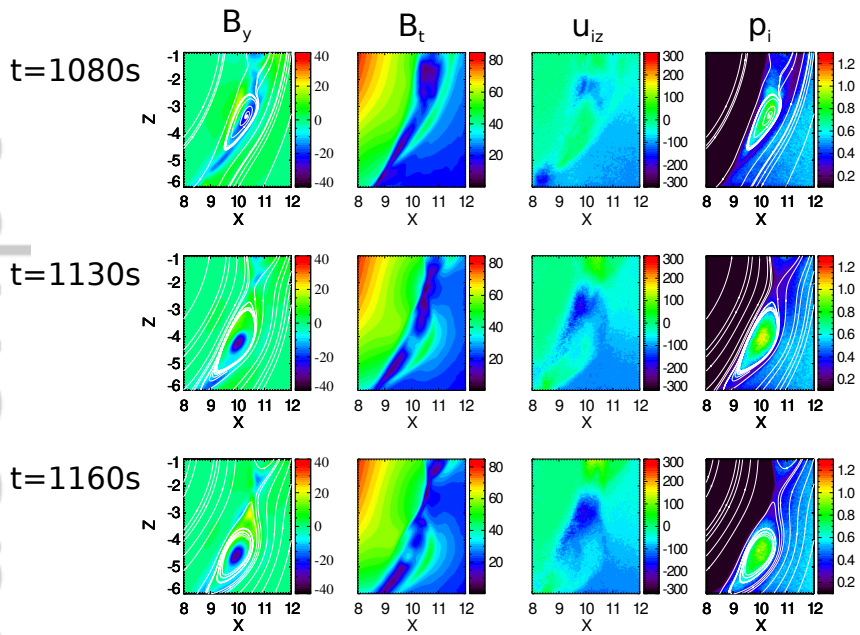
358 **Figure 5.** FTE dissipation crossing the southern cusp. A series of snapshots of current density $j_y[\mu\text{A}/\text{m}^2]$
 359 and field lines are shown. The plots are obtained from MHD output. Along the FTE's trajectory, the grid is
 360 uniform and the cell size is $1/16 R_E$. The red dashed line indicates the cut used in Figure 6



361 **Figure 6.** $j_y[\mu\text{A}/\text{m}^2]$ and $u_z[\text{km}/\text{s}]$ along the vertical red dashed line marked in Figure 5(c). The jump of
 362 u_z around $z \sim -9 R_E$ implies the occurrence of magnetic reconnection.

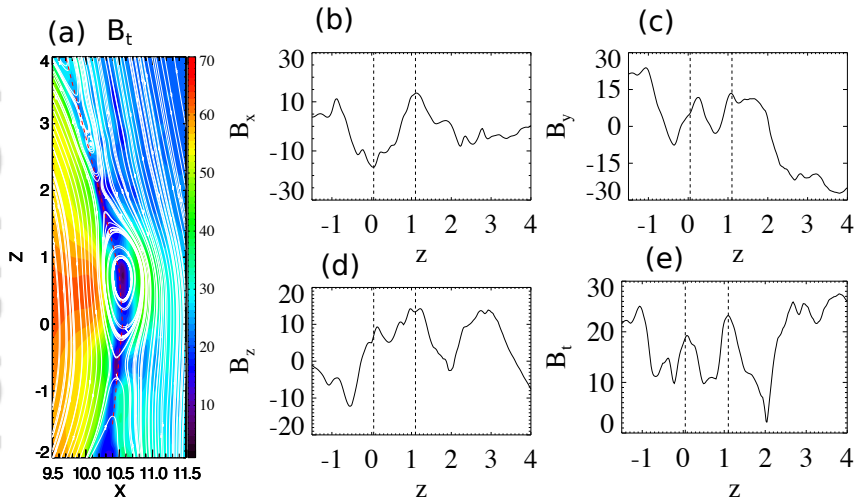


445 **Figure 7.** The evolution of FTEs in the meridional plane. From left to right, the four columns show
 446 the B_y [nT] and the projected magnetic field lines; the field strength B_t [nT]; the ion velocity in z direction
 447 U_{iz} [km/s]; and the ion pressure p_i [nPa] overlapped with magnetic field lines.



448

Figure 8. Same as Figure 7, except that the ion inertial length is scaled up by a factor of 32.



449

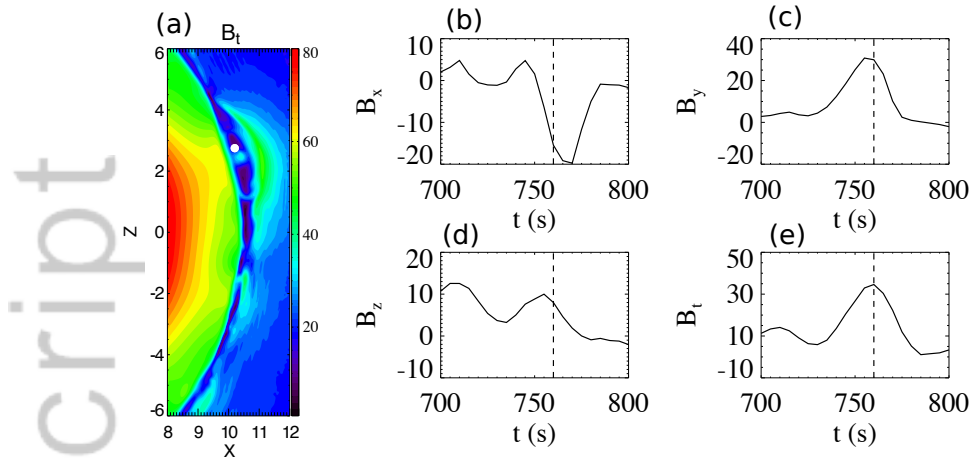
Figure 9. The crater flux rope at $t = 420$ s. The left panel shows the magnetic field strength and field

450

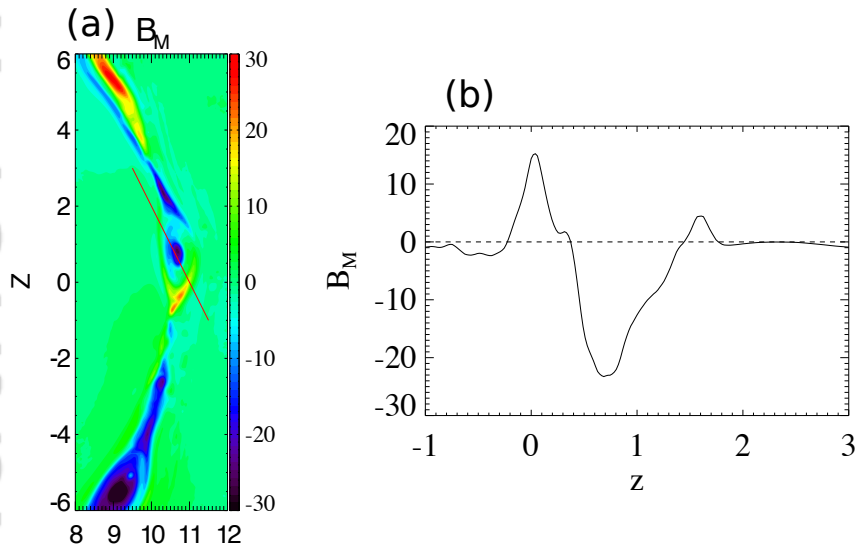
lines. The right four plots show the magnetic field along the red dashed line in the left panel. The two vertical

451

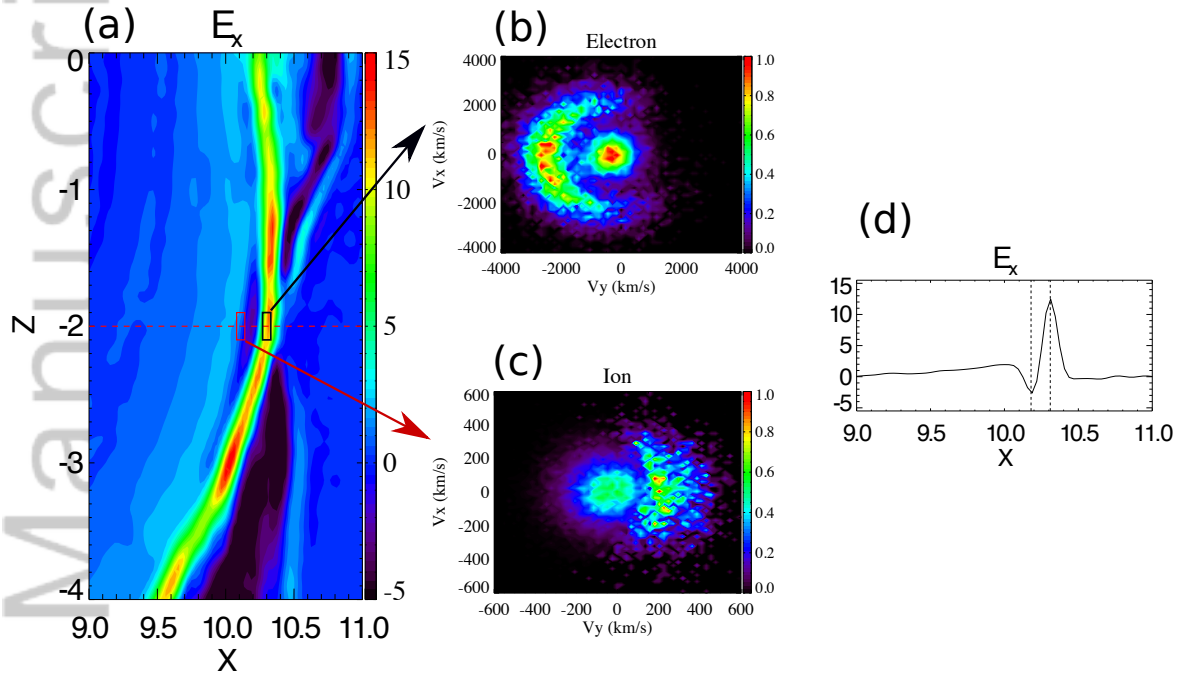
dashed lines represent the two peaks of B_x .



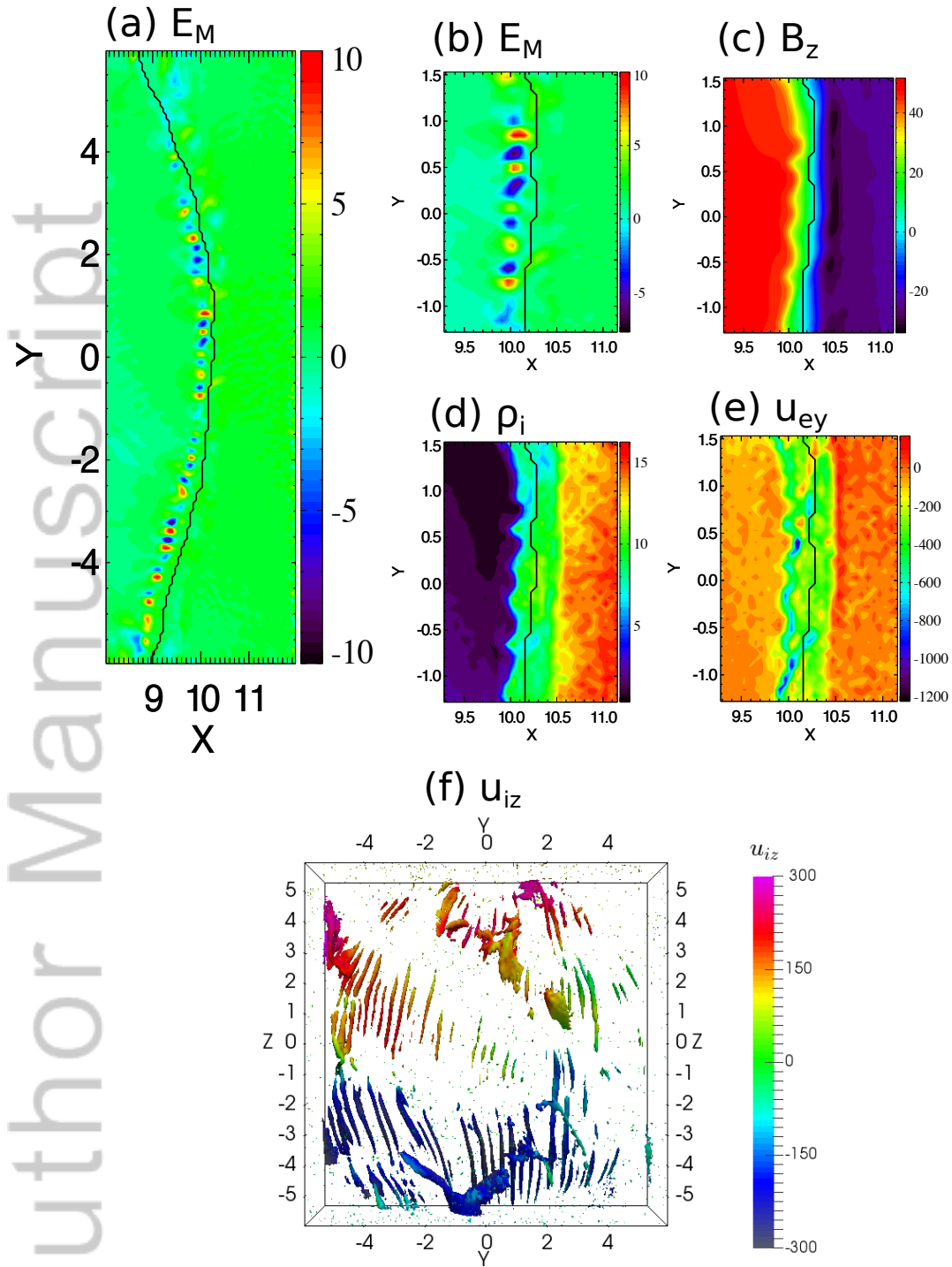
452 **Figure 10.** The magnetic field signature of a flux rope with significant core field. The left panel is the mag-
 453 netic field strength at $t = 740$ s. The white filled circle at $x = 10.2 R_E$, $z = 2.75 R_E$ is the location of the fixed
 454 virtual satellite. The right panels show the magnetic field observed by the satellite. The vertical dashed line at
 455 $t = 760$ s indicates the location of maximum B_t .



456 **Figure 11.** The tripolar guide field structure. The left panel shows the B_M component in the meridional
 457 plane at $t = 540$ s. Around the flux rope center, the guide field is negative, while the southern part of this
 458 flux rope is surrounded by the 'Y' shaped positive B_M . The field along the red solid line is shown in the right
 459 panel.



511 **Figure 12.** The Larmor electric field and crescent electron and ion phase space distributions. (a)
 512 E_x [mV/m] in the meridional plane at $t = 3600$ s. (b) The normalized electron distribution in $V_y - V_x$
 513 phase space. The electrons are inside the black box shown in (a): $10.27 R_E < x < 10.33 R_E, -0.3 R_E <$
 514 $y < 0.3 R_E, -2.1 R_E < z < -1.9 R_E$. (c) Ion phase space distribution for particles inside the red box in
 515 (a): $10.08 R_E < x < 10.14 R_E, -0.3 R_E < y < 0.3 R_E, -2.1 R_E < z < -1.9 R_E$. The phase density is
 516 normalized. (d) E_x along the red dashed line in panel (a).



547 **Figure 13.** The Lower hybrid drift instability (LHDI) at $t = 3600$ s. (a) Electric field E_M [mV/m] along the
 548 direction that is anti-parallel to the magnetopause current direction in the $z = -3 R_E$ plane. Near $y = 0$, the
 549 current direction is almost parallel to the y direction. (b)-(e): zoomed in view of different variables for LHDI
 550 at $z = -3 R_E$. (c) is the B_z field in nT, (d) is the ion density in amu/cm^3 and (e) is the electron velocity along
 551 y direction. The black curves in (a)-(e) separate the negative and positive B_z . (f) The 3D contour surface of
 552 $E_M = 4$ mV/m colored by the ion velocity along the z direction (u_{iz} [km/s]).

References

- Bessho, N., L.-J. Chen, and M. Hesse (2016), Electron distribution functions in the diffusion region of asymmetric magnetic reconnection, *Geophysical Research Letters*.
- Bode, B., M. Butler, T. Dunning, W. Gropp, T. Hoe-fler, W.-m. Hwu, and W. Kramer (2012), The blue waters super-system for super-science. contemporary hpc architectures, jeffery vetter editor.
- Burch, J. L., R. B. Torbert, T. D. Phan, L.-J. Chen, T. E. Moore, R. E. Ergun, J. P. Eastwood, D. J. Gershman, P. A. Cassak, M. R. Argall, S. Wang, M. Hesse, C. J. Pollock, B. L. Giles, R. Nakamura, B. H. Mauk, S. A. Fuselier, C. T. Russell, R. J. Strangeway, J. F. Drake, M. A. Shay, Y. V. Khotyaintsev, P.-A. Lindqvist, G. Marklund, F. D. Wilder, D. T. Young, K. Torkar, J. Goldstein, J. C. Dorelli, L. A. Avanov, M. Oka, D. N. Baker, A. N. Jaynes, K. A. Goodrich, I. J. Cohen, D. L. Turner, J. F. Fennell, J. B. Blake, J. Clemmons, M. Goldman, D. Newman, S. M. Petrinec, K. J. Trattner, B. Lavraud, P. H. Reiff, W. Baumjohann, W. Magnes, M. Steller, W. Lewis, Y. Saito, V. Coffey, and M. Chandler (2016), Electron-scale measurements of magnetic reconnection in space, *Science*, 352, 6290, doi:10.1126/science.aaf2939.
- Daldorff, L. K. S., G. Tóth, T. I. Gombosi, G. Lapenta, J. Amaya, S. Markidis, and J. U. Brackbill (2014), Two-way coupling of a global Hall magnetohydrodynamics model with a local implicit Particle-in-Cell model, *J. Comput. Phys.*, 268, 236, doi:10.1016/j.jcp.2014.03.009.
- Daly, P., D. Williams, C. Russell, and E. Keppler (1981), Particle signature of magnetic flux transfer events at the magnetopause, *Journal of Geophysical Research: Space Physics*, 86(A3), 1628–1632.
- Daughton, W. (2003), Electromagnetic properties of the lower-hybrid drift instability in a thin current sheet, *Physics of Plasmas*, 10(8), 3103–3119.
- Dorelli, J., and A. Bhattacharjee (2009), On the generation and topology of flux transfer events, *Journal of Geophysical Research: Space Physics*, 114(A6).
- Eastwood, J., T. Phan, R. Fear, D. Sibeck, V. Angelopoulos, M. Øieroset, and M. Shay (2012), Survival of flux transfer event (fte) flux ropes far along the tail magnetopause, *Journal of Geophysical Research: Space Physics*, 117(A8).
- Eastwood, J., T. Phan, P. Cassak, D. Gershman, C. Haggerty, K. Malakit, M. Shay, R. Mistry, M. Øieroset, C. Russell, et al. (2016), Ion-scale secondary flux ropes generated by magnetopause reconnection as resolved by mms, *Geophysical Research Letters*,

676 43(10), 4716–4724.

677 Eriksson, S., G. Lapenta, D. Newman, T. Phan, J. Gosling, B. Lavraud, Y. V. Khotyaintsev, C. Carr, S. Markidis, and M. Goldman (2015), On multiple reconnection x-lines and tripolar perturbations of strong guide magnetic fields, *The Astrophysical Journal*, 678 805(1), 43.

681 Eriksson, S., P. Cassak, A. Retinò, and F. Mozer (2016), Subsolar magnetopause observation and kinetic simulation of a tripolar guide magnetic field perturbation consistent with a magnetic island, *Geophysical Research Letters*, 43(7), 3035–3041.

684 Fear, R., S. Milan, A. Fazakerley, E. Lucek, S. Cowley, and I. Dandouras (2008), The azimuthal extent of three flux transfer events.

686 Fedder, J. A., S. P. Slinker, J. G. Lyon, and C. T. Russell (2002), Flux transfer events in global numerical simulations of the magnetosphere, *J. Geophys. Res.*, 107(A5), doi: 687 10.1029/2001JA000025.

689 Graham, D., Y. V. Khotyaintsev, C. Norgren, A. Vaivads, M. André, S. Toledo-Redondo, P.-A. Lindqvist, G. Marklund, R. Ergun, W. Paterson, et al. (2016), Lower hybrid waves in the ion diffusion and magnetospheric inflow regions, *Journal of Geophysical Research: Space Physics*.

693 Hasegawa, H., B. Ö. Sonnerup, C. Owen, B. Klecker, G. Paschmann, A. Balogh, and H. Rème (2006), The structure of flux transfer events recovered from cluster data, in *Annales Geophysicae*, vol. 24, pp. 603–618.

696 Hesse, M., K. Schindler, J. Birn, and M. Kuznetsova (1999), The diffusion region in collisionless magnetic reconnection, *Phys. Plasmas*, 6, 1781, doi:10.1063/1.873436.

698 Hesse, M., N. Aunai, D. Sibeck, and J. Birn (2014), On the electron diffusion region in planar, asymmetric, systems, *Geophysical Research Letters*, 41(24), 8673–8680.

700 Hoilijoki, S., U. Ganse, Y. Pfau-Kempf, P. A. Cassak, B. M. Walsh, H. Hietala, S. von Alfthan, and M. Palmroth (2017), Reconnection rates and x line motion at the magnetopause: Global 2d-3v hybrid-vlasov simulation results, *Journal of Geophysical Research: Space Physics*, pp. n/a–n/a, doi:10.1002/2016JA023709, 2016JA023709.

704 Huba, J., N. Gladd, and K. Papadopoulos (1977), The lower-hybrid-drift instability as a source of anomalous resistivity for magnetic field line reconnection, *Geophysical Research Letters*, 4(3), 125–128.

707 LaBelle, J., R. Treumann, G. Haerendel, O. Bauer, G. Paschmann, W. Baumjohann, H. Lüher, R. Anderson, H. Koons, and R. Holzworth (1987), Amplitude observations of

709 waves associated with flux transfer events in the magnetosphere, *Journal of Geophysical*
710 *Research: Space Physics*, 92(A6), 5827–5843.

711 Lapenta, G., S. Markidis, A. Divin, M. Goldman, and D. Newman (2010), Scales of guide
712 field reconnection at the hydrogen mass ratio, *Physics of Plasmas*, 17(8), 082,106, doi:
713 10.1063/1.3467503.

714 Lapenta, G., J. Berchem, M. Zhou, R. Walker, M. El-Alaoui, M. Goldstein, W. Paterson,
715 B. Giles, C. Pollock, C. Russell, et al. (2017), On the origin of the crescent-shaped
716 distributions observed by mms at the magnetopause, *Journal of Geophysical Research:*
717 *Space Physics*, 122(2), 2024–2039.

718 Lee, L. C., and Z. F. Fu (1985), A theory of magnetic flux transfer at the earth’s magne-
719 topause, *Geophysical Research Letters*, 12(2), 105–108, doi:10.1029/GL012i002p00105.

720 Malakit, K., M. A. Shay, P. A. Cassak, and D. Ruffolo (2013), New electric field in asym-
721 metric magnetic reconnection, *Physical review letters*, 111(13), 135,001.

722 Markidis, S., G. Lapenta, and Rizwan-Uddin (2010), Multi-scale simulations of
723 plasma with ipic3d, *Mathematics and Computers in Simulation*, 80, 1509–1519, doi:
724 10.1016/j.matcom.2009.08.038.

725 Mozer, F., M. Wilber, and J. Drake (2011), Wave associated anomalous drag during mag-
726 netic field reconnection, *Physics of Plasmas*, 18(10), 102,902.

727 Owen, C., A. Marchaudon, M. Dunlop, A. Fazakerley, J.-M. Bosqued, J. Dewhurst,
728 R. Fear, S. Fuselier, A. Balogh, and H. Reme (2008), Cluster observations of
729 “crater” flux transfer events at the dayside high-latitude magnetopause, *Journal*
730 *of Geophysical Research: Space Physics*, 113(A7).

731 Peng, I. B., S. Markidis, A. Vaivads, J. Vencels, J. Amaya, A. Divin, E. Laure, and
732 G. Lapenta (2015), The formation of a magnetosphere with implicit particle-in-cell sim-
733 ulations, *Procedia Computer Science*, 51, 1178–1187.

734 Powell, K., P. Roe, T. Linde, T. Gombosi, and D. L. De Zeeuw (1999), A solution-
735 adaptive upwind scheme for ideal magnetohydrodynamics, *J. Comput. Phys.*, 154, 284–
736 309, doi:10.1006/jcph.1999.6299.

737 Price, L., M. Swisdak, J. Drake, P. Cassak, J. Dahlin, and R. Ergun (2016), The effects of
738 turbulence on three-dimensional magnetic reconnection at the magnetopause, *Geophys-
739 ical Research Letters*, 43(12), 6020–6027.

740 Pritchett, P. (2013), The influence of intense electric fields on three-dimensional asymmet-
741 ric magnetic reconnection, *Physics of Plasmas*, 20(6), 061,204.

- 742 Raeder, J. (2006), Flux transfer events: 1. generation mechanism for strong southward imf,
743 *Annales Geophysicae*, 24, 381–392.
- 744 Ricci, P., J. U. Brackbill, W. Daughton, and G. Lapenta (2004), Collisionless magnetic
745 reconnection in the presence of a guide field, *Phys. Plasmas*, 11, 4102.
- 746 Ridley, A., T. Gombosi, and D. Dezeew (2004), Ionospheric control of the magneto-
747 sphere: conductance, *Annales Geophysicae*, 22, 567–584, doi:10.5194/angeo-22-567-
748 2004.
- 749 Rijnbeek, R., S. Cowley, D. Southwood, and C. Russell (1984), A survey of dayside flux
750 transfer events observed by ISEE 1 and 2 magnetometers, *J. Geophys. Res.*, 89, 786.
- 751 Roytershteyn, V., W. Daughton, H. Karimabadi, and F. Mozer (2012), Influence of the
752 lower-hybrid drift instability on magnetic reconnection in asymmetric configurations,
753 *Physical review letters*, 108(18), 185,001.
- 754 Russell, C., and R. Elphic (1978), Initial ISEE magnetometer results: Magnetopause ob-
755 servations, *Space Sci. Rev.*, 22, 681.
- 756 Shay, M., T. Phan, C. Haggerty, M. Fujimoto, J. Drake, K. Malakit, P. Cassak, and
757 M. Swisdak (2016), Kinetic signatures of the region surrounding the x line in asym-
758 metric (magnetopause) reconnection, *Geophysical Research Letters*, 43(9), 4145–4154.
- 759 Shay, M. A., and J. F. Drake (1998), The role of electron dissipation on the rate
760 of collisionless magnetic reconnection, *Geophys. Res. Lett.*, 25, 3759, doi:
761 10.1029/1998GL900036.
- 762 Shay, M. A., J. F. Drake, and M. Swisdak (2007), Two-scale structure of the electron dis-
763 sipation region during collisionless magnetic reconnection, *Phys. Rev. Lett.*, 99, 155,002,
764 doi:10.1103/PhysRevLett.99.155002.
- 765 Sibeck, D., M. Kuznetsova, V. Angelopoulos, K.-H. Glaßmeier, and J. McFadden (2008),
766 Crater ftes: Simulation results and themis observations, *Geophysical Research Letters*,
767 35(17).
- 768 Tóth, G., I. V. Sokolov, T. I. Gombosi, D. R. Chesney, C. Clauer, D. L. D. Zeeuw, K. C.
769 Hansen, K. J. Kane, W. B. Manchester, K. G. Powell, A. J. Ridley, I. I. Roussev, Q. F.
770 Stout, O. Volberg, R. A. Wolf, S. Sazykin, A. Chan, B. Yu, and J. Kóta (2005), Space
771 Weather Modeling Framework: A new tool for the space science community, *J. Geo-
772 phys. Res.*, 110, A12,226, doi:10.1029/2005JA011126.
- 773 Tóth, G., Y. J. Ma, and T. I. Gombosi (2008), Hall magnetohydrodynamics on block adap-
774 tive grids, *J. Comput. Phys.*, 227, 6967–6984, doi:10.1016/j.jcp.2008.04.010.

775 Tóth, G., B. van der Holst, I. V. Sokolov, D. L. D. Zeeuw, T. I. Gombosi, F. Fang, W. B.
776 Manchester, X. Meng, D. Najib, K. G. Powell, Q. F. Stout, A. Glocer, Y.-J. Ma, and
777 M. Opher (2012), Adaptive numerical algorithms in space weather modeling, *J. Comput.*
778 *Phys.*, *231*, 870–903, doi:10.1016/j.jcp.2011.02.006.

779 Tóth, G., X. Jia, S. Markidis, B. Peng, Y. Chen, L. Daldorff, V. Tenishev, D. Borovikov,
780 J. Haiducek, T. Gombosi, A. Glocer, and J. Dorelli (2016), Extended magnetohydro-
781 dynamics with embedded particle-in-cell simulation of ganymede’s magnetosphere, *J.*
782 *Geophys. Res.*, *121*, doi:10.1002/2015JA021997.

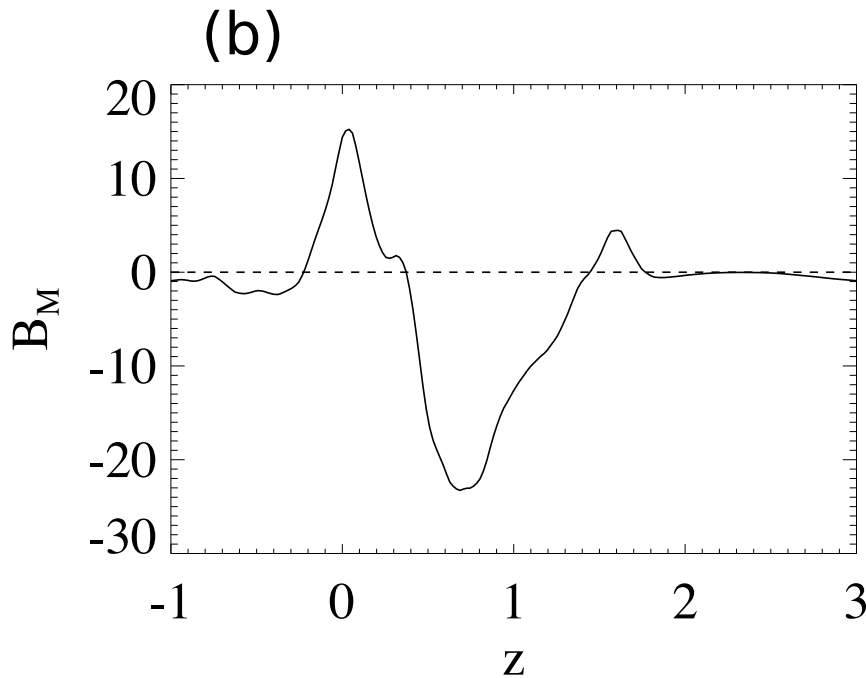
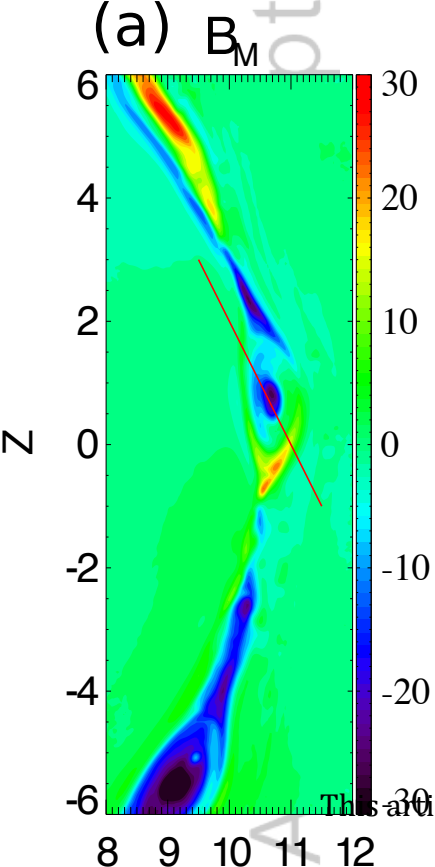
783 Tóth, G., Y. Chen, T. I. Gombosi, P. Cassak, , S. Markidis, and B. Peng (2017, submitted
784 paper), Scaling the ion inertial length and its implications for modeling reconnection in
785 global simulations, *J. Geophys. Res.*

786 Wang, C.-P., M. Gkioulidou, L. R. Lyons, and V. Angelopoulos (2012), Spatial distribu-
787 tions of the ion to electron temperature ratio in the magnetosheath and plasma sheet,
788 *Journal of Geophysical Research: Space Physics*, *117*(A8).

789 Zhang, H., M. Kivelson, K. Khurana, J. McFadden, R. Walker, V. Angelopoulos, J. Wey-
790 gand, T. Phan, D. Larson, K. Glassmeier, et al. (2010), Evidence that crater flux transfer
791 events are initial stages of typical flux transfer events, *Journal of Geophysical Research:*
792 *Space Physics*, *115*(A8).

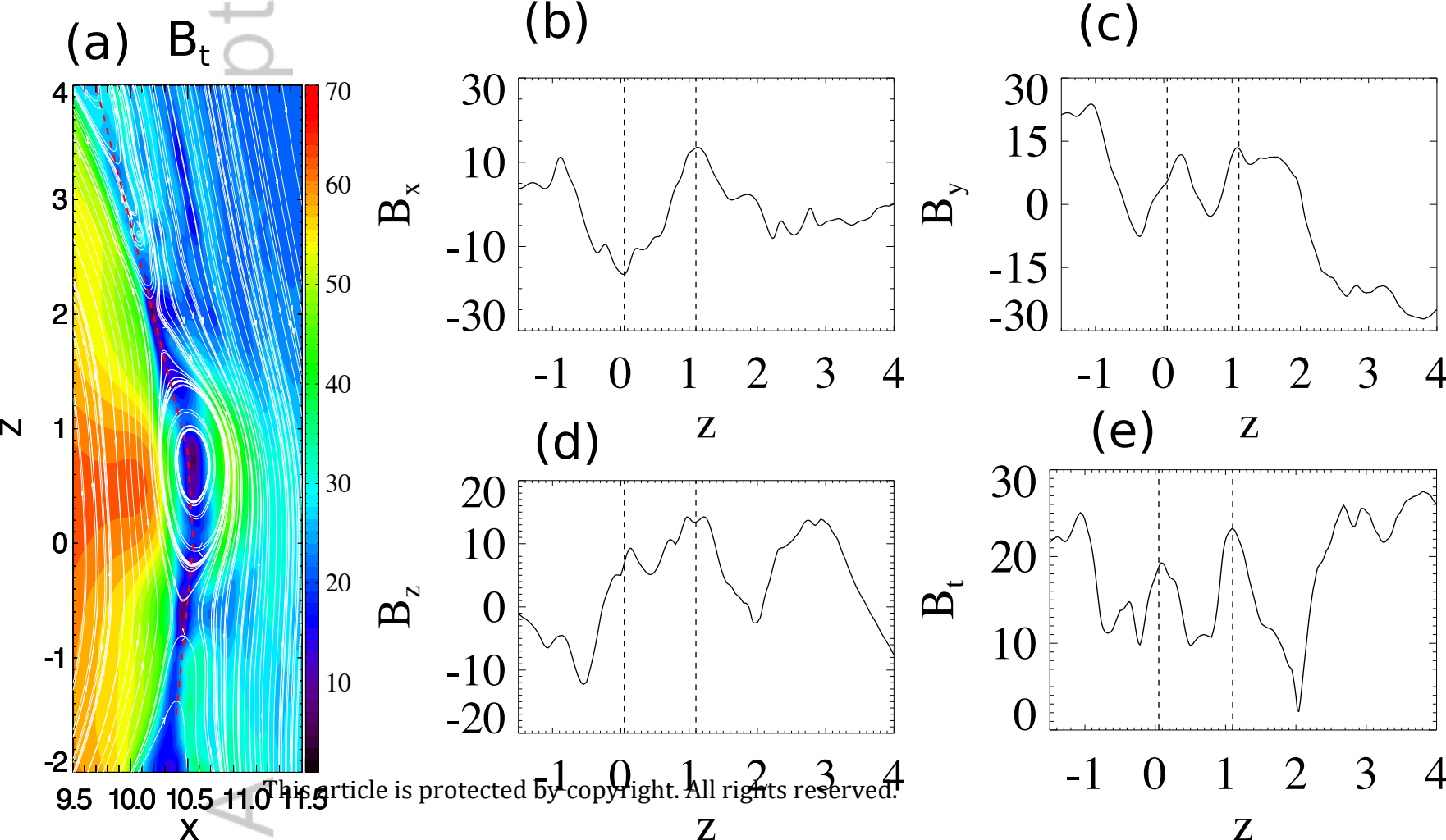
Author Manuscript

Author Manuscript

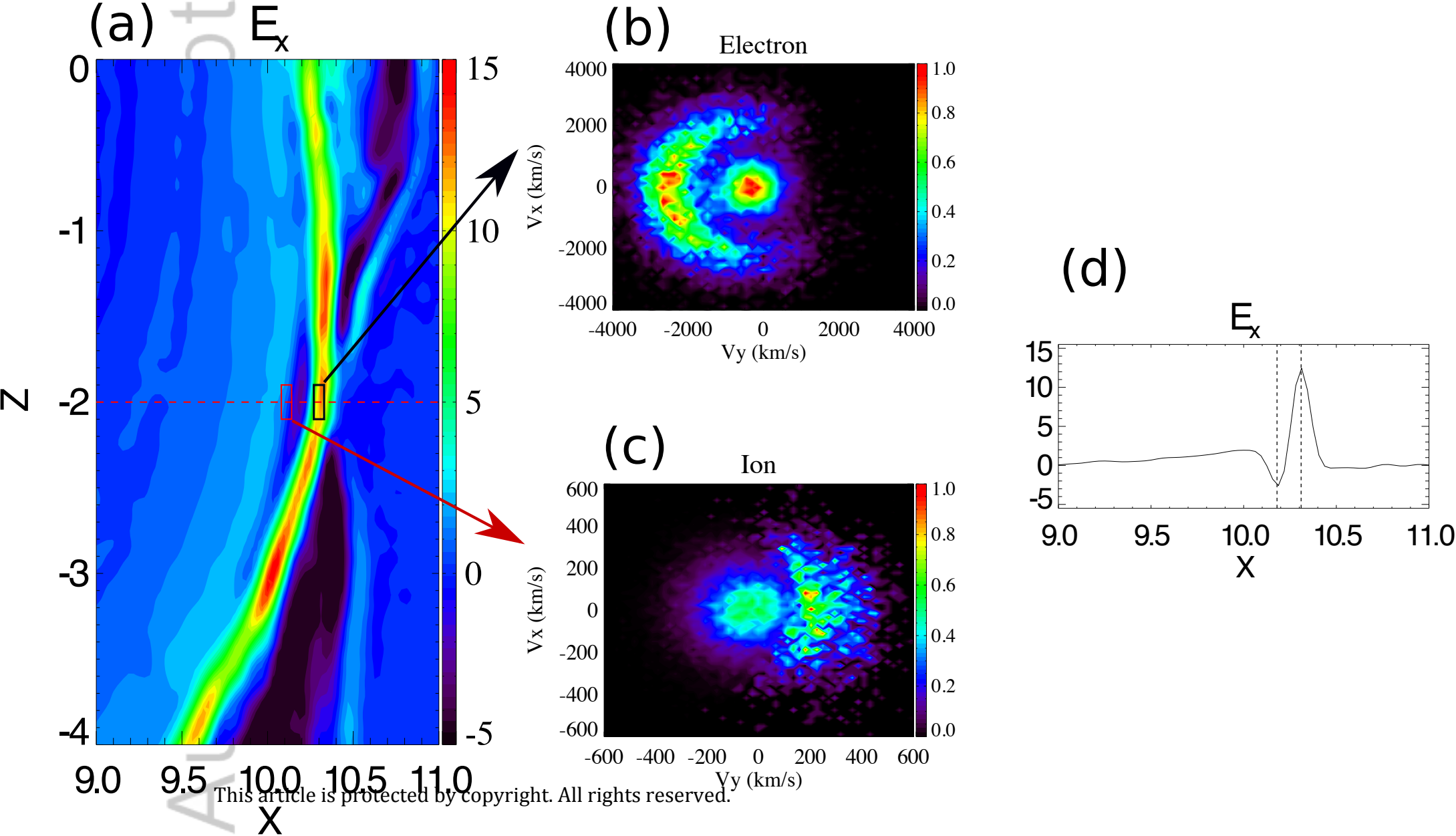


This article is protected by copyright. All rights reserved.

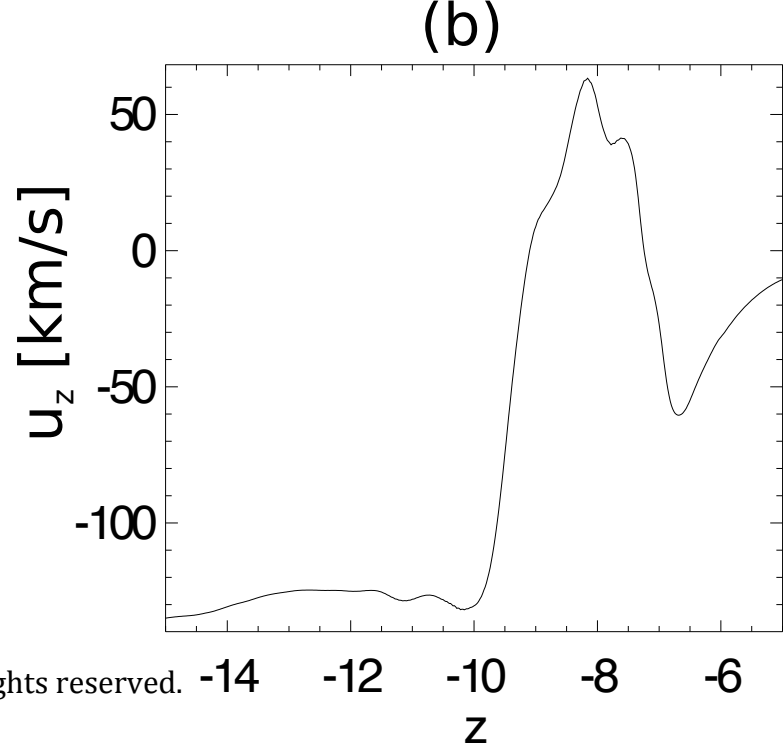
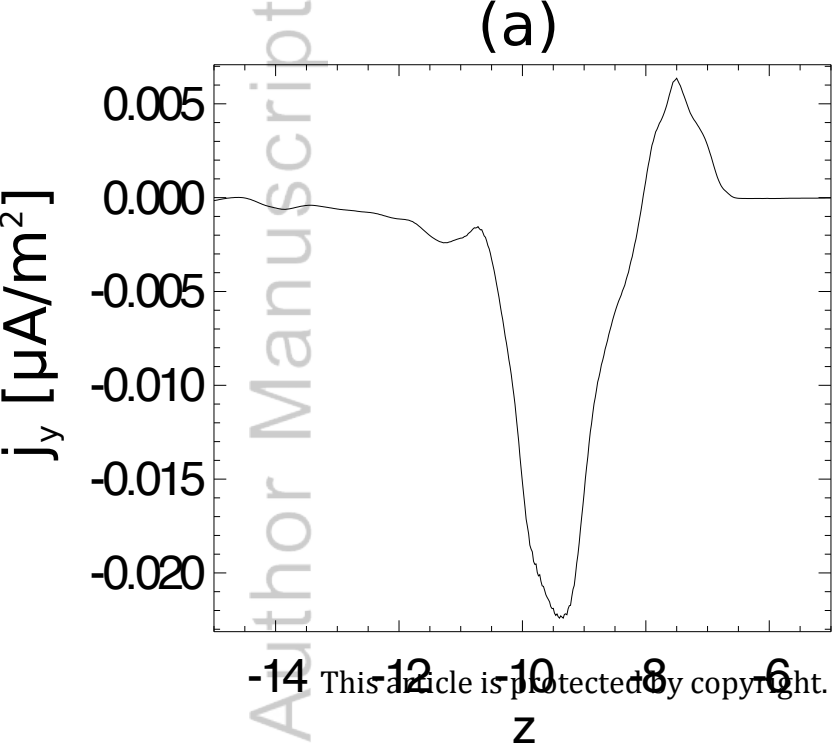
Author Manuscript



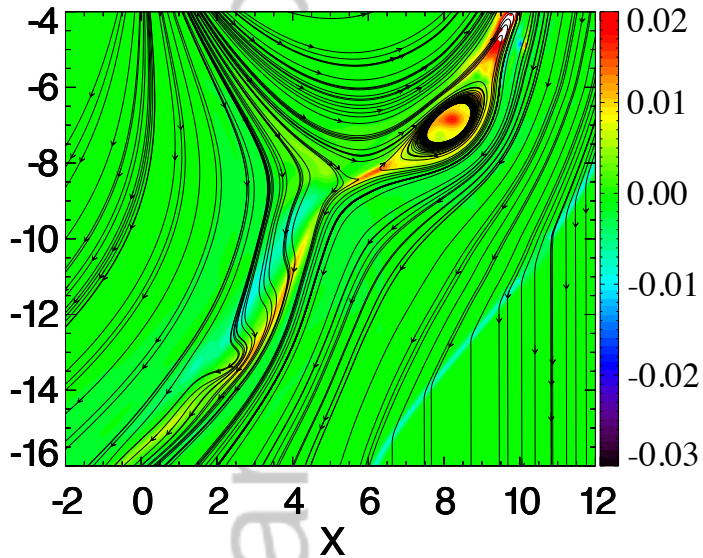
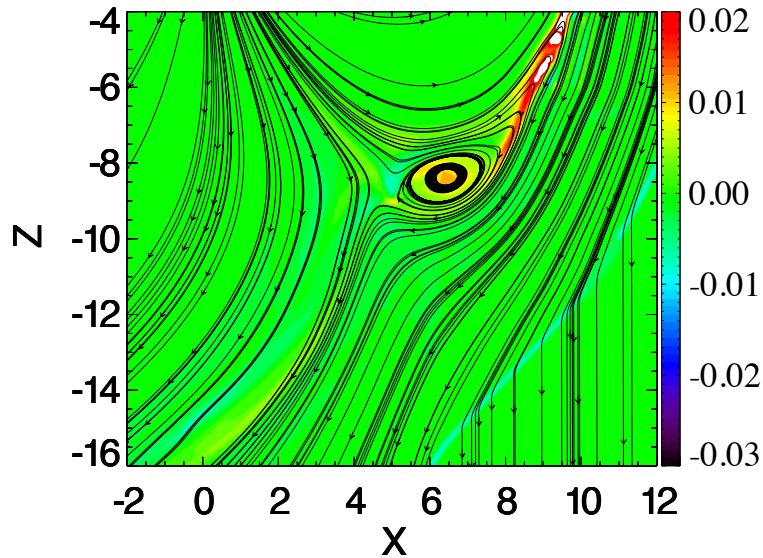
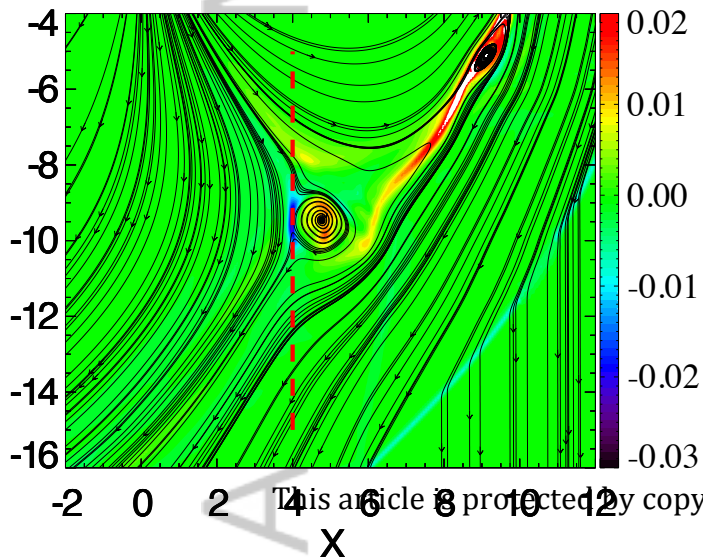
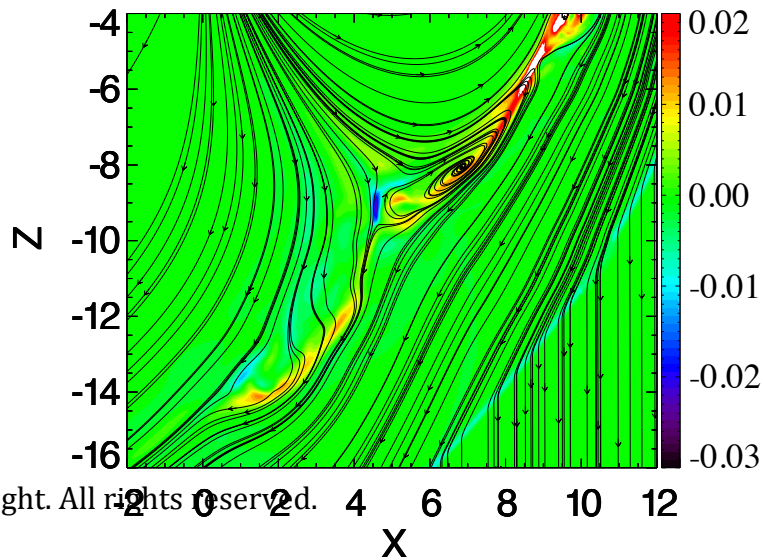
Author Manuscript



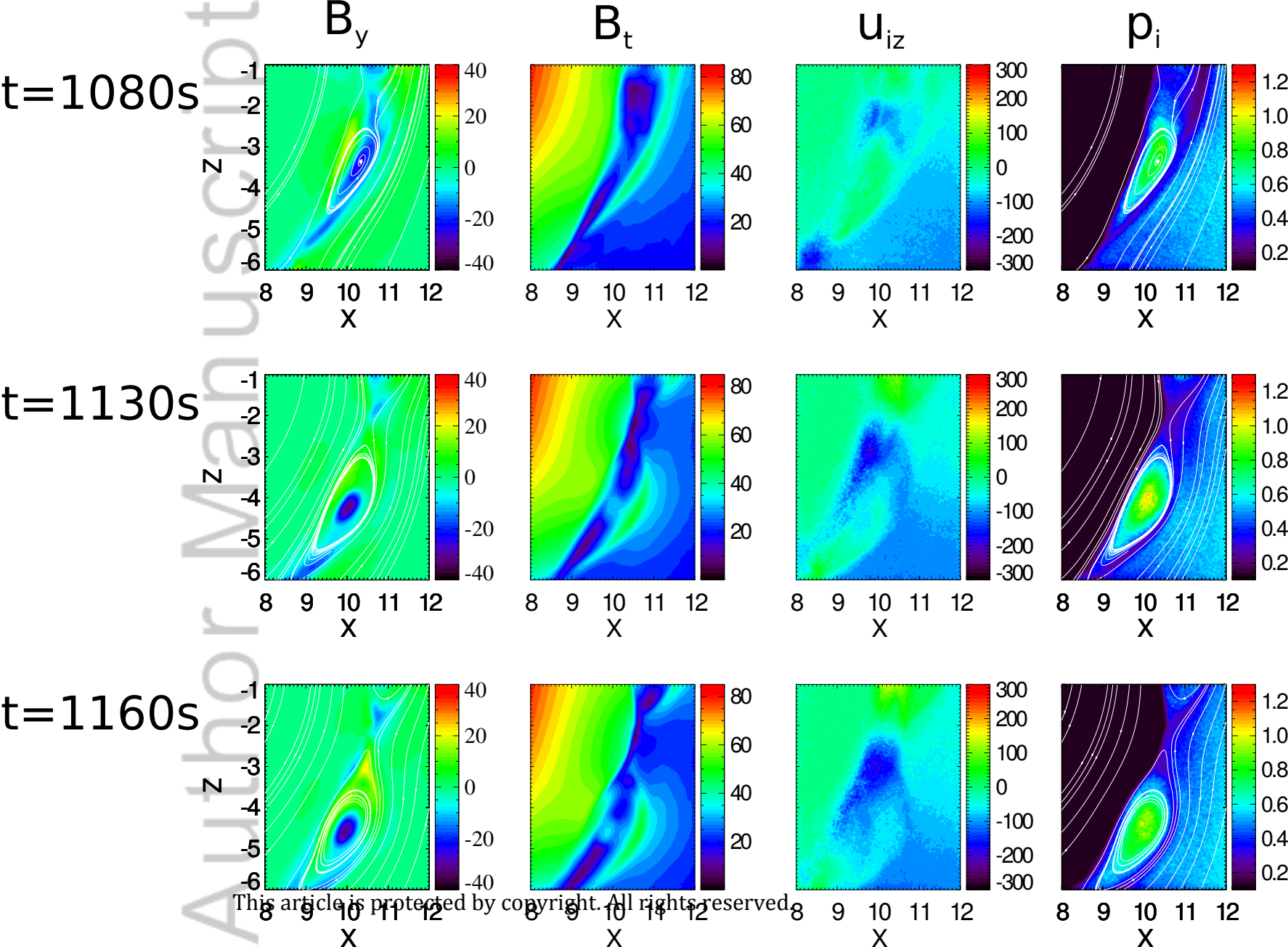
Author Manuscript



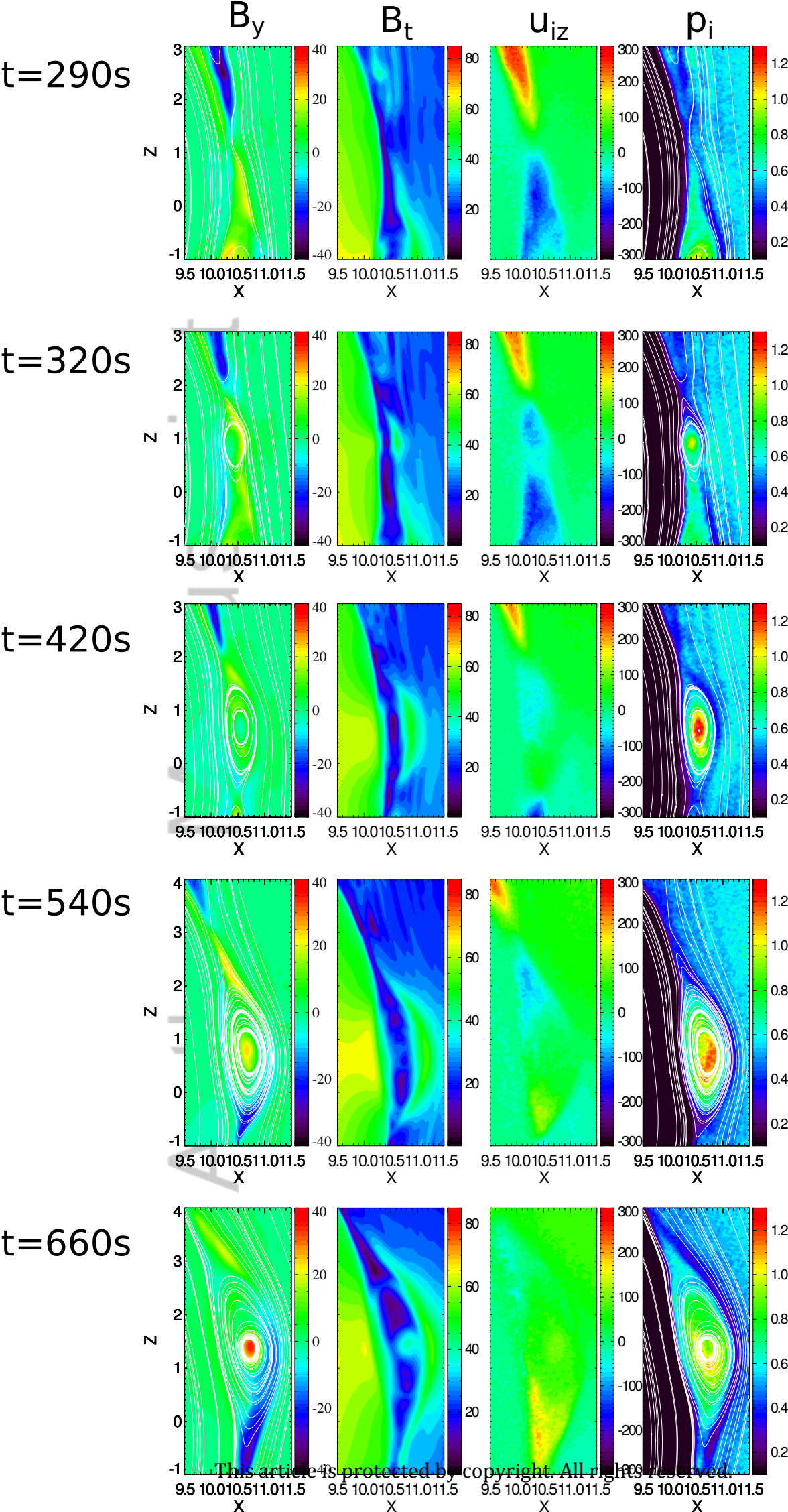
Author Manuscript

(a) $t = 600$ s(b) $t = 660$ s(c) $t = 720$ s(d) $t = 840$ s

Author Manuscript

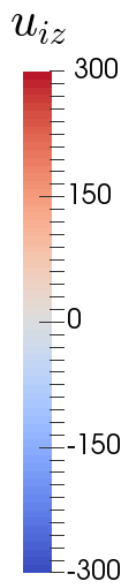
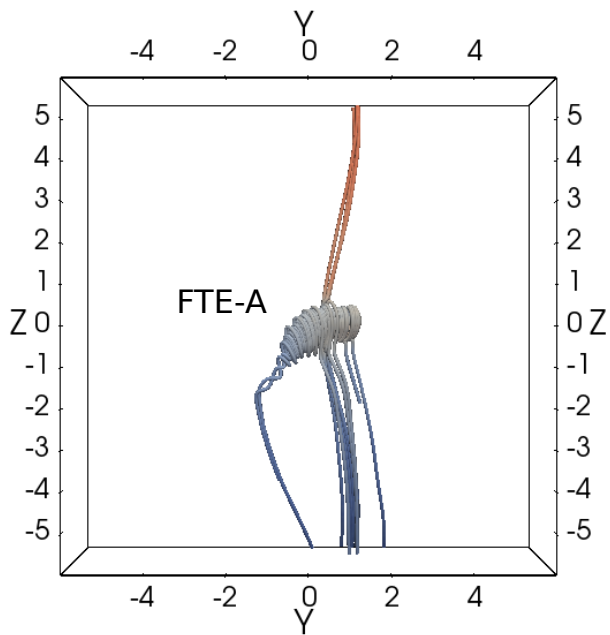


Author Manuscript

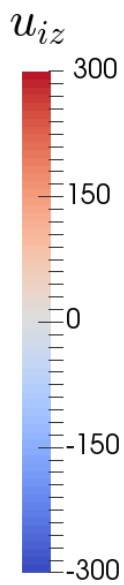
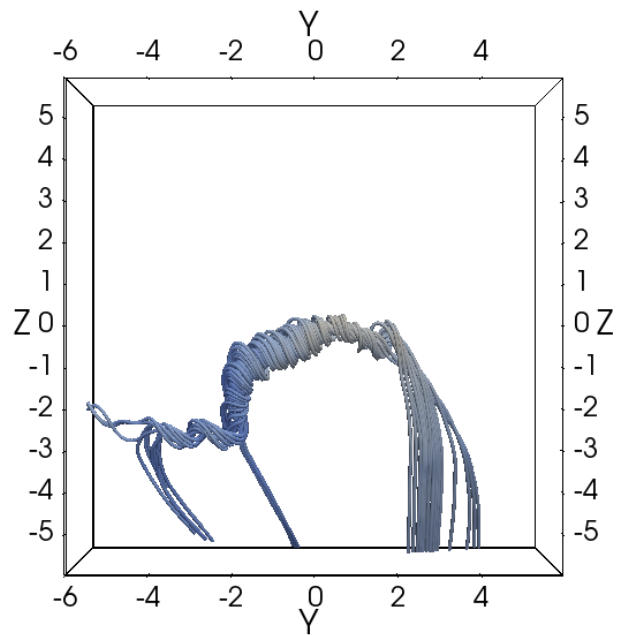


Author Manuscript

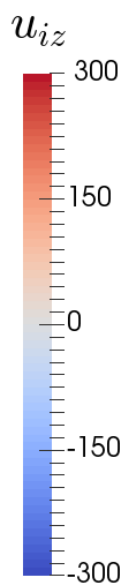
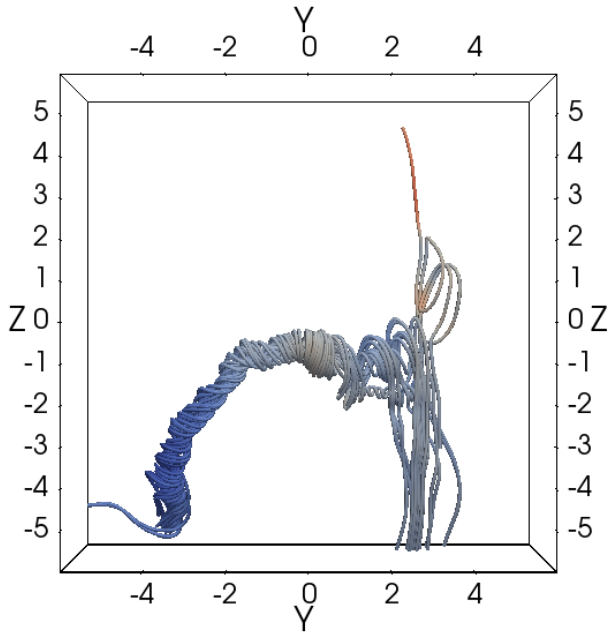
t=100s



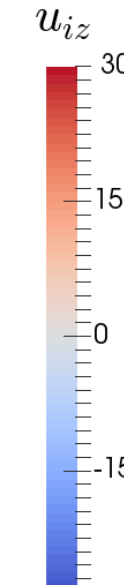
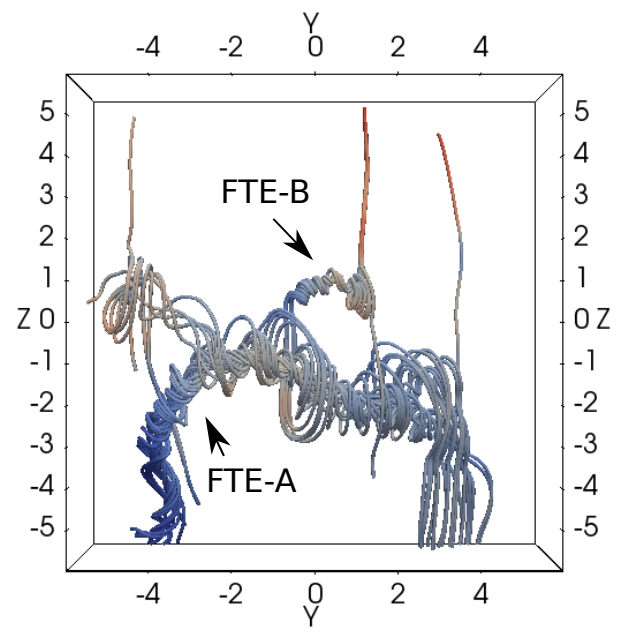
t=150s



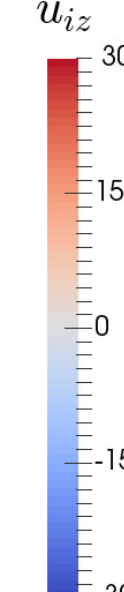
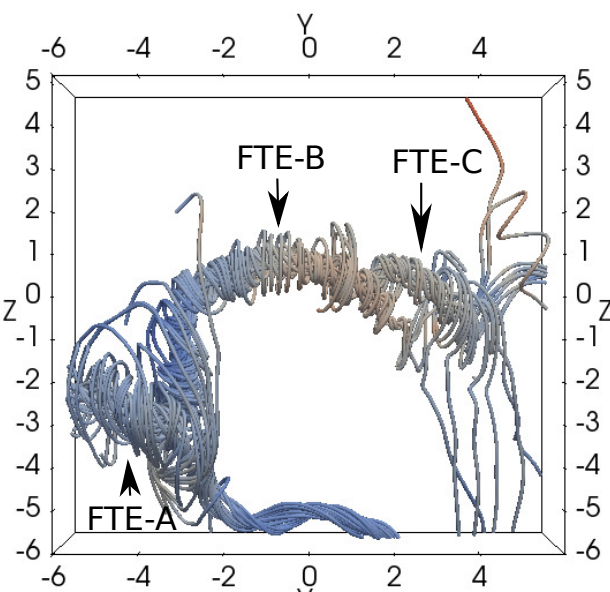
t=240s



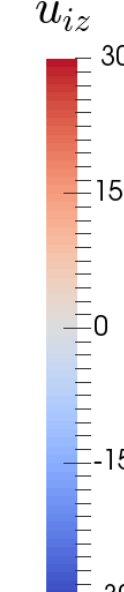
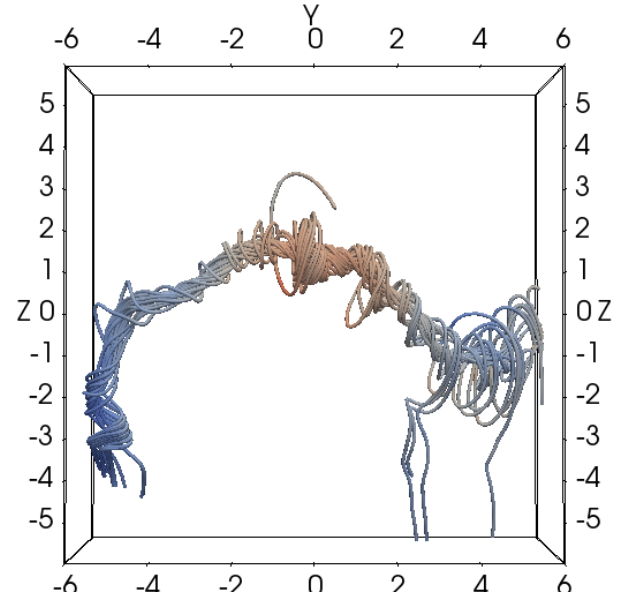
t=320s



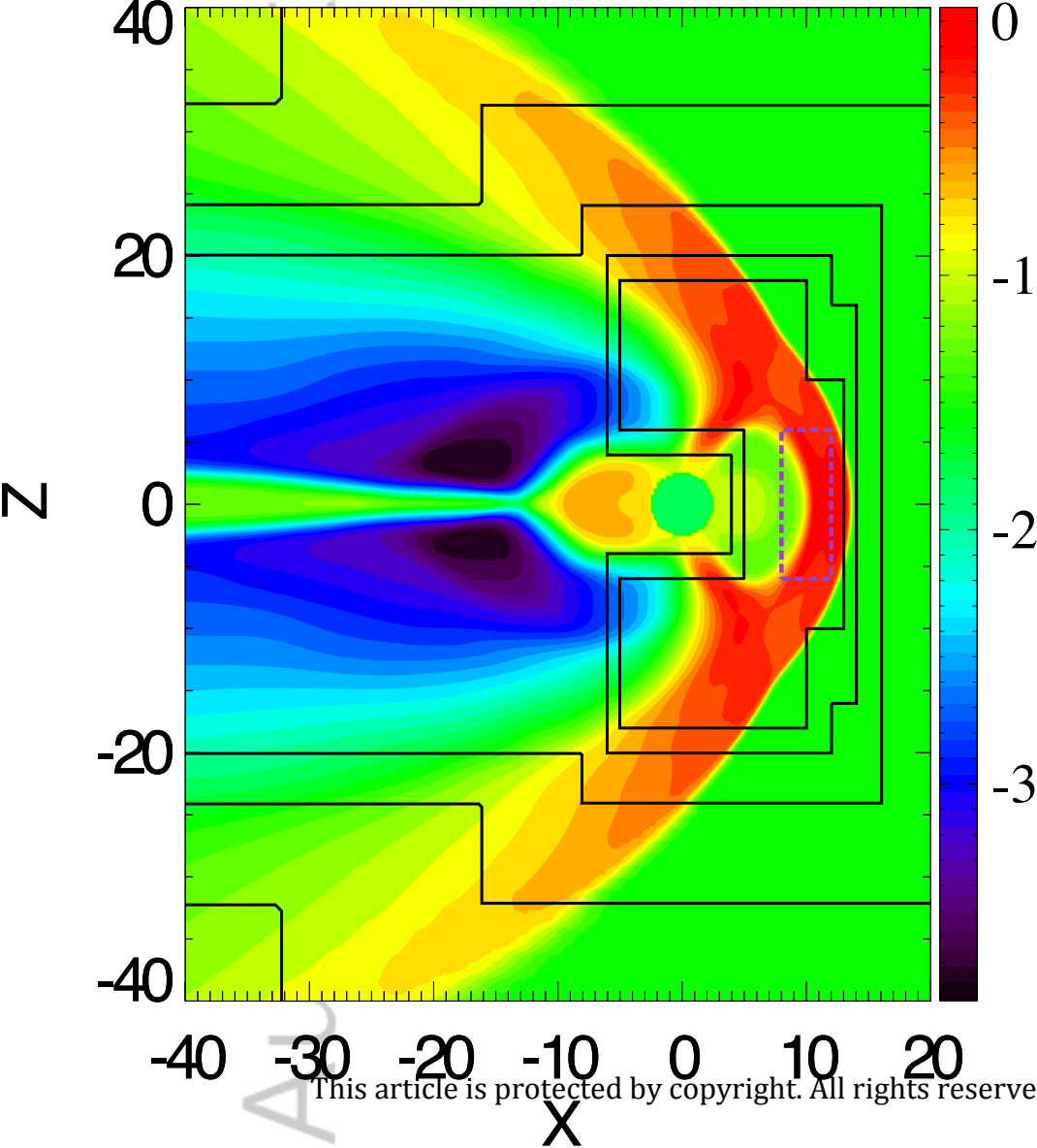
t=540s



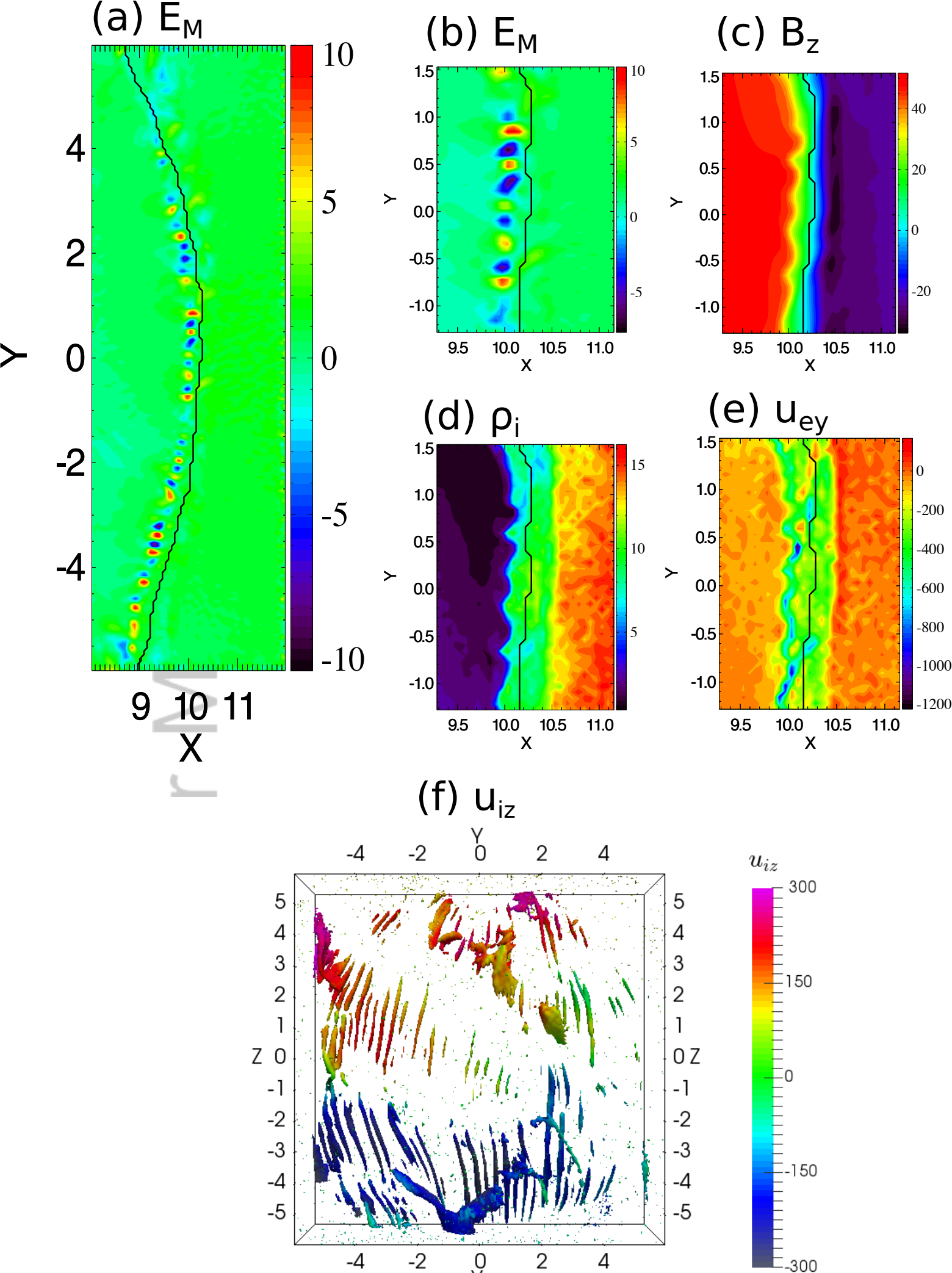
t=660s



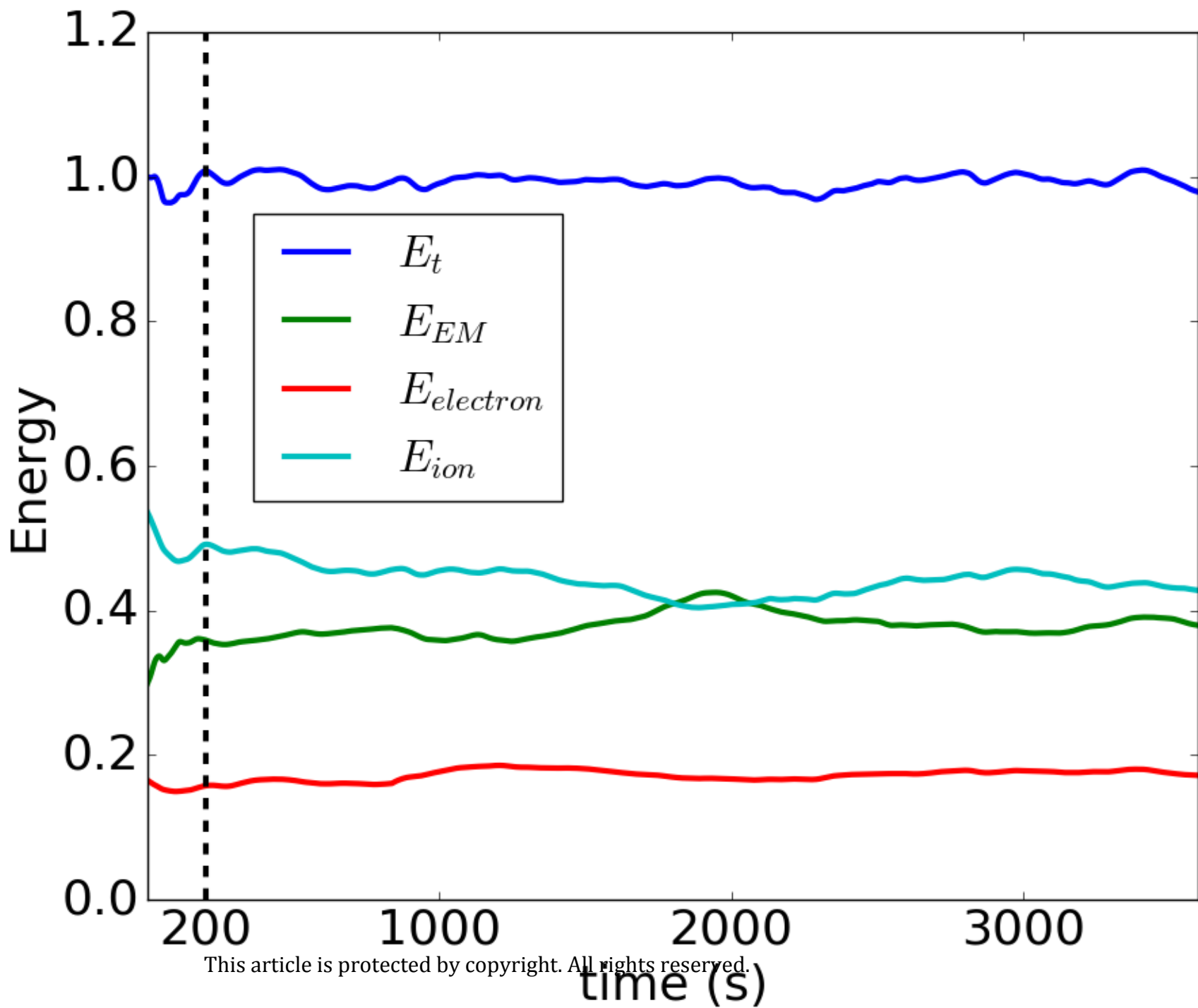
Author Manuscript



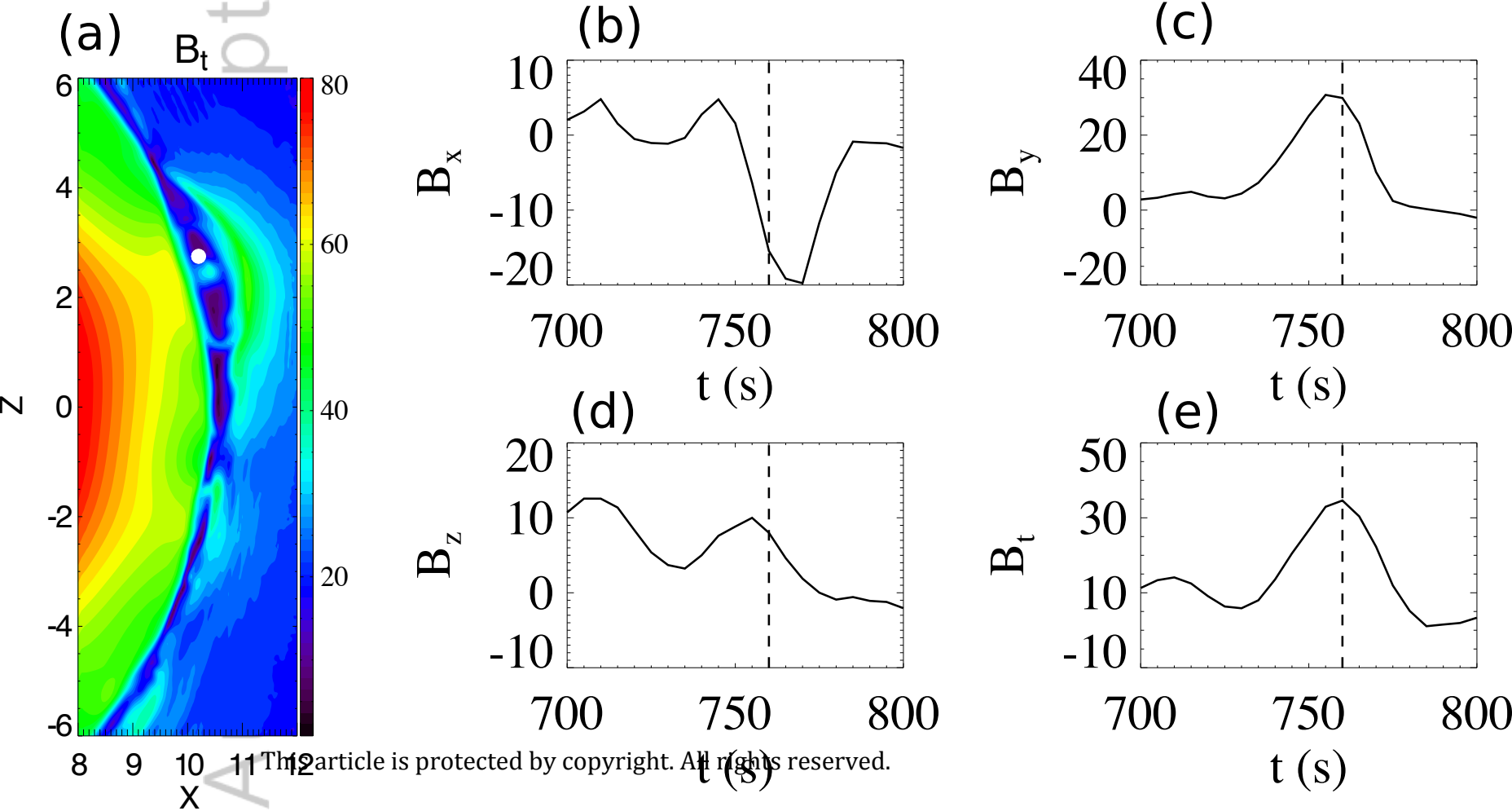
Author Manuscript



Author Manuscript

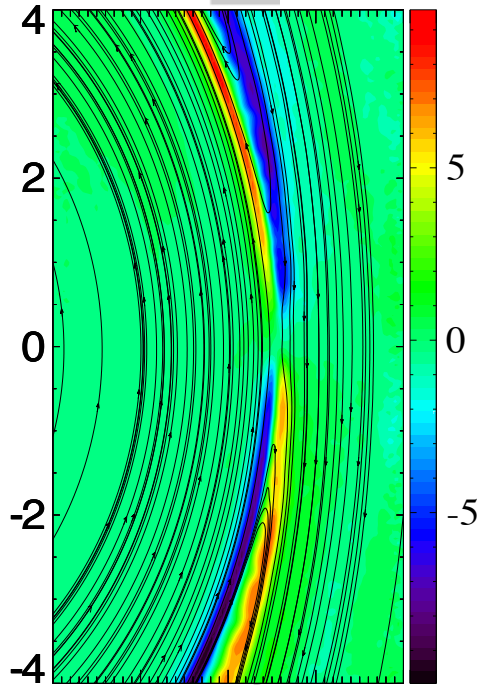


Author Manuscript

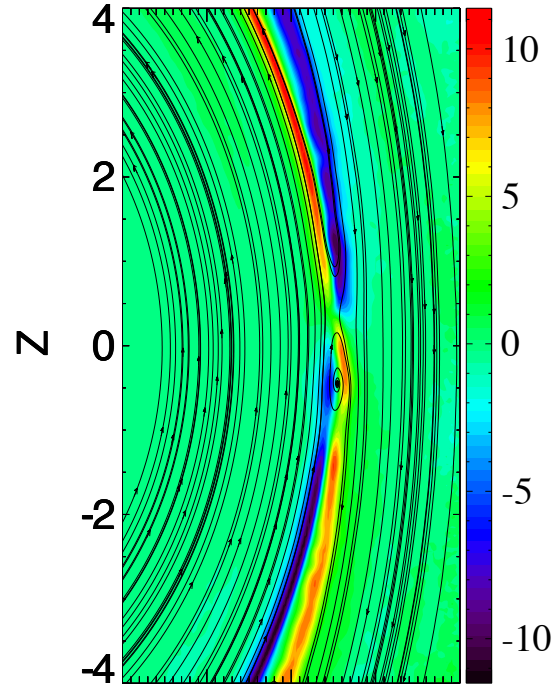


Author Manuscript

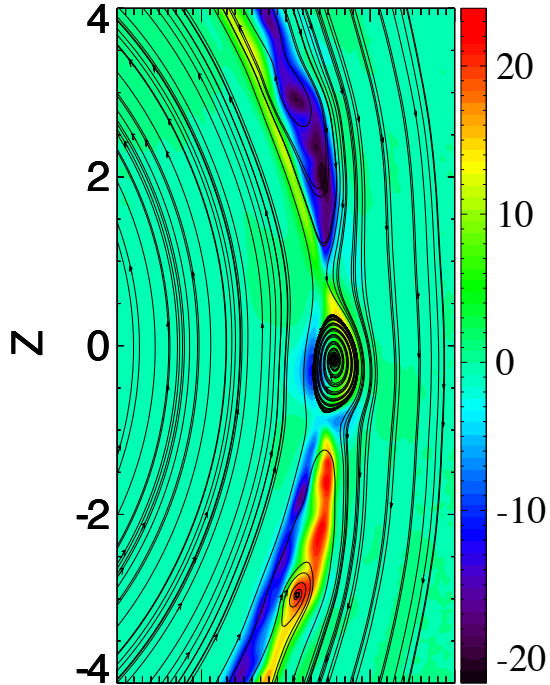
$t = 70 \text{ s}$



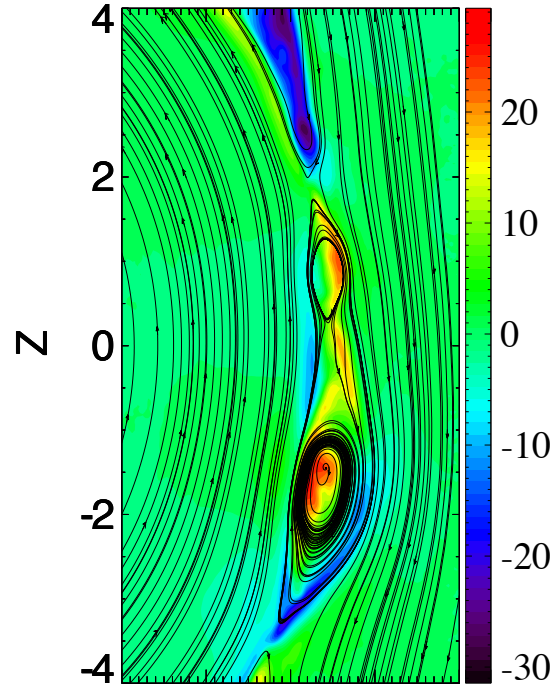
$t = 85 \text{ s}$



$t = 145 \text{ s}$



$t = 325 \text{ s}$



This article is protected by copyright. All rights reserved.